Canadian Science Publishing

ARTICLE

Landfast ice properties over the Beaufort Sea region in 2000–2019 from MODIS and Canadian Ice Service data[1]

Alexander P. Trishchenko, Vladimir E. Kostylev, Yi Luo, Calin Ungureanu, Dustin Whalen, and Junhua Li

Abstract: Two decades (2000–2019) of the landfast ice properties in the Beaufort Sea region in the Canadian Arctic were analyzed at 250 m spatial resolution from two sources: (1) monthly maps derived at the Canada Centre for Remote Sensing from the Moderate Resolution Imaging Spectroradiometer clear-sky satellite image composites; and (2) Canadian Ice Service charts. Detailed comparisons have been conducted for the landfast ice spatial extent, the water depth at, and the distance to the outer seaward edge from the coast in four sub-regions: (1) Alaska coast; (2) Barter Island to Herschel Island; (3) Mackenzie Bay; and (4) Richards Island to Cape Bathurst. The results from both sources demonstrate good agreement. The average spatial extent for the entire region over the April–June period is 48.5 ($\pm$5.0) $\times$ 10^3 km^2 from Canadian Ice Service data versus 45.1 ($\pm$6.1) $\times$ 10^3 km^2 from satellite data used in this study (7.0% difference). The correlation coefficient for April–June is 0.73 (p = 2.91 $\times$ 10^{-4}). The long-term linear trends of the April–June spatial extent since 2000 demonstrated statistically significant decline: $-$4.45 ($\pm$1.69) $\times$ 10^3 km^2/decade and $-$4.73 ($\pm$2.17) $\times$ 10^3 km^2/decade from Canadian Ice Service and satellite data, respectively. The landfast ice in the Beaufort Sea region showed the general tendency for an earlier break-up, later onset, and longer ice-free period. The break-up date has decreased by 7.6 days/decade in the Mackenzie Bay region. The western part of the study area did not demonstrate statistically significant changes since 2000.

Key words: landfast ice, Beaufort Sea, Mackenzie Bay, Canadian Arctic, satellite data.

Résumé : Les propriétés sur deux décennies (2000–2019) de la banquise côtière dans la région de la mer de Beaufort, dans l'Arctique canadien, ont été analysées à une résolution spatiale de 250 m à partir de données de deux sources, soit (1) des cartes mensuelles dérivées au Centre canadien de télédétection d'images satellites composites par ciel clair du spectroradiomètre imageur à résolution moyenne et (2) des cartes du Service canadien des glaces. Des comparaisons détaillées ont été menées pour l'étendue spatiale de la banquise côtière, la profondeur de l'eau et la distance jusqu'au bord extérieur de la banquise côtière vers la mer à partir de la côte dans quatre sous-régions, dont (1) le littoral de l'Alaska, (2) de l'île Barter à l'île Herschel, (3) la baie Mackenzie et (4) de l'île Richards au cap Bathurst. Les résultats tirés des deux sources concordent bien. L'étendue spatiale moyenne pour toute la région pendant la période d'avril à juin est de 48,5 ($\pm$5,0) $\times$ 10^3 km^2 selon les données du Service canadien des glaces et de 45,1 ($\pm$6,1) $\times$ 10^3 km^2 selon les données satellites utilisées dans l'étude (une différence de 7,0 %). Le coefficient de corrélation pour avril à juin est de 0,73 (p = 2,91 $\times$ 10^{-4}). Les tendances linéaires à long terme de l'étendue spatiale d'avril à juin depuis 2000 reflètent une diminution statistiquement significative, de $-$4,45 ($\pm$1,69) $\times$ 10^3 km^2/décennie et $-$4,73 ($\pm$2,17) $\times$ 10^3 km^2/décennie pour les données du Service canadien des glaces et les données satellites, respectivement. La banquise côtière dans la région de la mer de Beaufort présente une tendance générale vers une dislocation plus hâtive, une prise plus tardive et une plus longue période libre de glace. La dislocation de la glace est devancée à raison de 7,6 jours/décennie dans la région de la baie Mackenzie. La partie occidentale de la région à l'étude ne présente pas de changement statistiquement significatif depuis l'année 2000. [Traduit par la Rédaction]

Mots-clés : banquise côtière, mer de Beaufort, baie Mackenzie, Arctique canadien, données satellites.

Introduction

Landfast ice (LFI), also known as shore-fast ice, primarily forms in shallow coastal waters. The definition of the LFI is provided by the World Meteorological Organization (WMO) in the document "Sea Ice List of symbols" (WMO 2014). It is also included in the Manual of Ice (MANICE 2009) compiled by the Canadian Ice Service (CIS). The LFI is generally defined as ice that is attached to the shore, to the bottom of the sea or to the ice wall or grounded icebergs. It may consist of first-year or multi-year ice and can spread from a few metres to several hundred kilometres. The LFI extends along the entire coast of the Beaufort Sea during the cold season and a large part of the summer and represents an important component of the Beaufort Sea climate system (Mahoney 2018). It occupies most of

Received 21 January 2021. Accepted 13 September 2021.

A.P. Trishchenko, C. Ungureanu, and J. Li. Canada Centre for Remote Sensing, Natural Resources Canada, Ottawa, ON K1A 0E4, Canada.
V.E. Kostylev and D. Whalen. Geological Survey Canada – Atlantic, Natural Resources Canada, Dartmouth, NS B2Y 4A2, Canada.
Y. Luo. Canadian Ice Service, Environment and Climate Change Canada, Ottawa, ON K1A 0H3, Canada.
Corresponding author: Alexander P. Trishchenko (email: alexander.trichtchenko@nrcan-rncan.gc.ca).

[1]This paper is part of a Special Issue entitled "Landscape and Seascape Responses to Canada's Changing Climate", which brings together articles that describe and quantify the landscape of Canada and adjacent regions in the face of a changing climate.

the Canadian Arctic archipelago area in the winter season. The LFI zone serves as an important area that supports the traditional and cultural livelihood of the Inupiat and Inuit people, many Arctic communities, and wildlife ecosystems. It provides transportation routes for fishing, hunting, and communications between remote and isolated communities, as well as other sea-ice-related services for several months each year (Ford et al. 2009; Gearheard et al. 2006; Huntington et al. 2016; Mahoney 2018; Eicken et al. 2009). It is also an important factor in regulating erosion rates of coastline because the loss of sea ice enhances wave action (Overeem et al. 2011).

The LFI is built tightly into the chain of ecosystem functions and services. It serves as important habitat for marine mammals (Laidre and Regehr 2016; Laidre et al. 2008). The enhanced ecological productivity has been also observed under the LFI and its seaward edge (Mundy et al. 2009, 2014). The impact of climate change on LFI is considered to be one of the most significant factors affecting the Arctic coastal communities and the movement of marine mammals (Loseto et al. 2018; Cooley et al. 2020). It is a well-known fact that the Arctic is warming at a rate almost twice the global average (Overland et al. 2019). This warming trend has a significant impact on LFI extent, formation, and break-up. The timing of LFI break-up controls the travel patterns and accessibility of beluga whales to the coastal zone. This is an important subsistence species for the Inuvialuit people in the region (Loseto et al. 2018). As such, quantitative information about the spatial and temporal dynamics of coastal zone LFI is needed to better assess the impacts of climate change in the Arctic.

The Global Climate Observing System generally requires spatial resolution of 1–5 km and weekly temporal frequency for sea ice extent/edge products (GCOS 2016). The operational sea-ice mapping, including the LFI, is conducted by specialized national agencies, such as the CIS (https://www.canada.ca/en/environment-climate-change/services/ice-forecasts-observations.html) and the U.S. National Ice Center (https://www.navcen.uscg.gov/?pageName=NationalIceCenter). These agencies generate daily and weekly products that represent the best estimate of ice properties produced by an integration of data from multiple sources of information including spaceborne, airborne, and marine observations (ECCC 2020; Tivy et al. 2011). The U.S. National Snow and Ice Data Center in collaboration with the U.S. National Ice Center generates the daily 4 km and 1 km sea-ice products over the Northern Hemisphere termed the Multi-sensor Analyzed Sea Ice Extent - Northern Hemisphere (Fetterer et al. 2010).

The historical archives of ice charts and maps from the national agencies serve as a good source of data for deriving LFI climatology and long-term trends. For example, Galley et al. (2012) analyzed the timing of LFI conditions in the Canadian Arctic for the period of 1983–2009 using the CIS ice charts. They rasterized data to a 2 km × 2 km grid and identified LFI using the total sea-ice concentration labelled as 10/10ths following recommendations from Melling (2002) and Tivy et al. (2011). Galley et al. (2012) have reported statistically significant trends for LFI onset (later start by 2.78 weeks/decade) and break-up (earlier start by 0.65 week/decade) in the Beaufort Sea. Yu et al. (2014) have analyzed the variations of LFI extent in the Arctic coastal areas for 1976–2007 from weekly sea-ice charts provided by the U.S. National Ice Center. The input data were digitally rasterized to the Equal Area Scalable Earth Grid format at 25 km spatial resolution (Brodzik and Knowles 2002). The mean LFI extent for the entire Beaufort Sea region in winter (January–May) was found to be 50.04×10^3 km^2, with an absolute negative trend at $-0.39\ (\pm 0.16) \times 10^3$ km^2 year^{-1} or a relative negative trend at $-7.79\ (\pm 3.20)$%/decade for the annual mean area over the 1976–2007 period. Li et al. (2020*b*) used the methodology developed by Yu et al. (2014) and extended a similar analysis to the 1976–2018 interval and the same 25 km spatial resolution. The ice charts produced by the Arctic and Antarctic Research Institute in St. Petersburg (Borodachev 1998) and mapped on 12.5 km grid have been utilized by Divine et al. (2003) to analyze the LFI extent in the northeastern part of the Kara Sea from 1953 to 1990.

The LFI has been studied at higher resolution with satellite data from the Synthetic Aperture Radar (SAR) and optical/thermal systems, such as Sentinel-2, LANDSAT, and WorldView (Barry et al. 1979; Karvonen 2018; Li et al. 2020*a*; Mäkynen et al. 2020). Dammann et al. (2019) used Sentinel-1 interferometry to map the pan-Arctic LFI in spring 2017. They utilized image pairs to map three LFI categories: (1) bottomfast ice, (2) stabilized floating LFI, and (3) nonstabilized floating coastal ice. This study emphasized the importance of considering the dynamic LFI stability rather than near-instantaneous ice concentration maps because these may lack sufficient information related to ice mobility at the highest concentration level 10/10th.

Mahoney et al. (2014) conducted a very comprehensive study of LFI in the Chukchi Sea and the western areas of the Beaufort Sea up to Mackenzie Bay using SAR imagery for the period of 1996–2008. By extending their previous research (Mahoney et al. 2007*a*, 2007*b*), they reported the mean width of the LFI zone in the western part of the Beaufort Sea in April to be about 31 km. In the Chukchi Sea, it was close to 14 km. They detected positive trends in the LFI freeze-up time and negative trends in break-up time, i.e., shorter duration of the LFI existence in this region. The above results related to the LFI spatial scale derived from high-resolution satellite data, clearly demonstrated that the application of 25 km spatial resolution data for LFI studies in the Beaufort Sea region could be questionable due to insufficient ability to resolve the LFI spatial features.

This paper extends our research on the application of the Moderate Resolution Imaging Spectroradiometer (MODIS) 250 m clear-sky composites produced at the Canada Centre for Remote Sensing (CCRS) (Luo et al. 2008; Trishchenko and Luo 2021). Trishchenko and Luo (2021) developed a method to delineate the LFI using monthly mean and standard deviation maps of MODIS reflectances. They produced a 20-year time series of LFI properties for the Banks Island area and compared them with the CIS charts. The comparison demonstrated good agreement between the MODIS-based CCRS and the CIS results. The average correlation coefficients between the CIS and the CCRS time series of LFI properties were within 0.87–0.88. The relative differences (CIS minus CCRS) of LFI spatial extent, the ocean depth at the LFI edge. and the width of the LFI zone ranged from 6.3% to 10%. The current paper advances the application of the developed method to the entire Beaufort Sea area with a detailed analysis for several sub regions along the southern coast. In addition, it conducts the correlation analysis of derived time series with surface-level air temperatures from the European ERA5 reanalysis (Hersbach et al. 2020).

The application of the CCRS MODIS composites for LFI mapping was initially inspired by the observation of a well-identified zone, closely matching the 20–30 m isobaths, with an increased probability of sea-ice presence along the Beaufort Sea coastline (Figs. 1*a*–1*b*). A strong relationship between the location of the 20 m isobath and the average boundary of the LFI zone has been reported for Banks Island (Trishchenko and Luo 2021) and the western part of the Beaufort Sea region (Mahoney et al. 2014). The seasonally aggregated probability maps can serve as a useful proxy for the general location of the LFI zone in the Beaufort Sea region. However, due to the dynamic nature of LFI, these results are true only in a qualitative climatological sense, and the better characterization of LFI properties requires more detailed temporal resolution.

The main objective of this study is to improve the characterization of LFI properties (total area, water depth at outer edge, and its distance from shore) over the Beaufort Sea and its subregions along the southern coast by extending the method developed by Trishchenko and Luo (2021) to gain a better understanding of multi-year LFI properties and trends in the Beaufort Sea region.

Fig. 1. Region of interest in the Beaufort Sea. (*a*) 2000–2019 snow/ice probability maps for the melting season (April–September); (*b*) 2000–2019 mean snow/ice probability map with overlaid boundaries of five subregions and 20 and 30 m isobaths; (*c*) the ocean floor bathymetry and surface elevation map (GEBCO Bathymetric Compilation Group 2020). Five subregions are selected: 1, Alaska coast; 2, Barter Island to Hershel Island stretch; 3, Mackenzie Bay; 4, Richards Island to Cape Bathurst stretch; 5, Banks Island. The digital shapefile for the Beaufort Sea boundary was obtained from the open database published by the Flanders Marine Institute (2019). The Beaufort Sea boundary (*b*–*c*) follows the International Hydrographic Organization definition (IHO 1953).

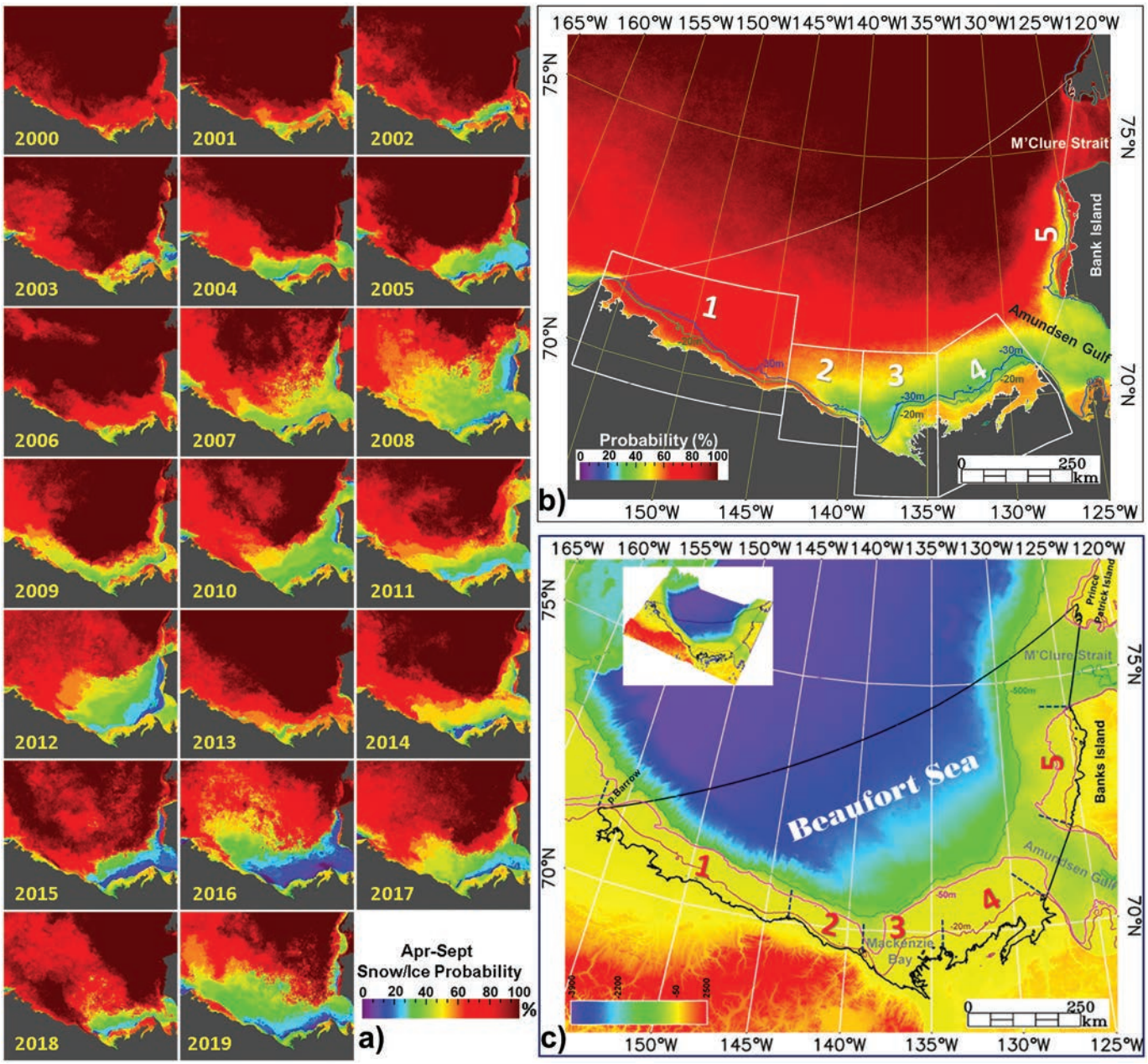

Results are based on the 250 m resolution maps derived for the 20-year period: 2000–2019. To our knowledge, this is the first time that LFI in the entire area of the Beaufort Sea is studied at 250 m spatial resolution for such a long time span using data independent of operational ice products. Previous long-term studies utilized data with a very coarse spatial resolution (grid size of 25 km × 25 km), which raises questions about their ability to adequately describe the LFI cover as the typical size of spatial features is much smaller than grid cell size. Available high-resolution studies do not provide similar spatial and (or) temporal coverage for the entire Beaufort Sea area. Comparison of independent data with the CIS ice charts can provide important insights into the potential uncertainties of the operational product. Results are also useful for improving the knowledge of multi-year LFI trends in the Beaufort Sea region since 2000.

Study region

The coastal ice regime in the Beaufort Sea region (Figs. 1*a*–1*c*) is generally driven by the bathymetry of the ocean floor in the shallow water zone, by a large-scale ocean circulation system persistent over the region called the Beaufort Gyre (Proshutinsky et al. 2002) and by the seasonal meteorological cycle. The central zone of the Beaufort Sea (Canada Basin) is deeper than 2000 m, while shallow (<100 m) shelf and coastal waters extend tens of kilometres

from shore (Fig. 1*c*). The variability in sea ice spatial distribution over the region (Fig. 1*a*) reflects interannual variations in the properties of the Beaufort Gyre and associated meteorological conditions. The 2012 summer minimum sea-ice cover in the region (Fig. 1*a*) occurred as a result of anomalously large solar absorption combined with some other factors (Babb et al. 2016). Reduced summer sea-ice cover in 2008 and 2016 can be also observed. Babb et al. (2019, 2020) found a link between the Beaufort Gyre reversal and the preceding summer sea-ice minimum in 2016. This reversal caused eastward ice motion in the region, leading to convergence of sea ice in the vicinity of Banks Island. The overall reduction of the summer sea-ice cover over the western Beaufort Sea observed in Fig. 1*a* is consistent with observations made by Steele et al. (2015). They reported that, in recent years, the sea ice in this area has become younger and thinner that resulted in an earlier break-up. Also, the date of ice cover retreat, when concentration falls below 15%, tends to occur earlier, although the trend is not statistically significant (Steele et al. 2015).

Once the LFI is formed, its general dynamics are mostly controlled by thermodynamic factors (Barry et al. 1979). The outer seaward ice edge is affected by the ocean surface conditions (waves) and currents, as well as atmospheric circulation that transfers energy and momentum fluxes to sea ice (Carmack and Chapman 2003).

Five subregions of the Beaufort Sea were selected for detailed analysis. Region 1 (Alaska coast) stretches from Point Barrow to Barter Island. There is no well-defined LFI zone on the multi-year average probability map for this region (Fig. 1*b*). This reflects the complexity of coastal zone ice dynamics in this area and explains why the LFI delineation based on optical satellite images can be quite challenging in this region. Region 2 stretches from Barter Island to Hershel Island. The increased probability of the coastal sea ice is pronounced relatively well here. The characteristic feature of this region is the narrow shallow zone with water depths less than 30 m (Figs. 1*b*–1*c*). Region 3 (Mackenzie Bay) is a shallow zone bordering the Mackenzie River delta, known for its prominent economic and ecological significance. The Mackenzie River provides the largest fresh water and sediment input into the Arctic Ocean from the North American continent. Region 4 extends from Richards Island to Cape Bathurst. It has a well-defined zone of an increased presence of coastal ice that closely follows the 20 m isobath. This zone is slightly wider than in other regions. The Banks Island coastal zone (Region 5) demonstrates a very good example of the near-shore sea ice separated from the interior Beaufort Sea ice field by a distinct low-probability zone (mostly open water). It has a sharp outer gradient line that closely follows the 20–30 m isobaths. We do not specifically discuss results for the Banks Island region in this paper, as they can be found in Trishchenko and Luo (2021).

Data

CCRS MODIS composite products

The primary source of satellite data for this study is the MODIS imager operated by the U.S. National Aeronautics and Space Administration (NASA) on the TERRA spacecraft. This is one of the most advanced sensors utilized for a wide range of land, ocean, and atmosphere applications (Salomonson et al. 1989). The instrument includes 36 spectral bands with spatial resolution ranging from 250 m to 1 km at nadir. The MODIS bands 1 (B1, visible) and 2 (B2, near-infrared) are available at 250 m spatial resolution; an additional five spectral bands in the solar spectrum (bands B3 to B7) are available at 500 m spatial resolution. The remaining 29 bands have 1 km spatial resolution at nadir. Two MODIS instruments are currently operational: (1) MODIS on TERRA spacecraft and (2) MODIS on AQUA spacecraft. The regular MODIS observations begun in early 2000. They continue to the present time with daily coverage of the globe.

This study utilizes the MODIS clear-sky composite products over Canada that are produced at the CCRS from the original MODIS Level 1 (1B) swath data distributed by NASA (https://ladsweb.modaps.eosdis.nasa.gov/). The MODIS 500 m bands (B3–B7) are downscaled to 250 m spatial resolution (same as of bands B1 and B2) using adaptive regression and normalization scheme (Trishchenko et al. 2006). They are re-projected into regular map projection using the method of Khlopenkov and Trishchenko (2008). The re-projected images for bands B1–B7 are composited as 10-day (3 per month, 36 per year) clear-sky products for Canada and the Northern Circumpolar area using a clear-sky, cloud, and cloud shadow detection technique developed by Luo et al. (2008) and Trishchenko et al. (2009). The data from the MODIS sensor on TERRA but not on AQUA satellite are regularly processed in this study because the latter has substantial band-to-band misalignment and a significant number of dead detectors (Khlopenkov and Trishchenko 2008; Xiong et al. 2005, 2006). Clear-sky composites are produced separately for the backward (i.e., sun-satellite relative azimuth angle range −90° to 90°) and the forward (sun-satellite relative azimuth angle range of 90° to 270°) scattering directions.

The main intended use of the CCRS clear-sky composites is for land applications (Beaudoin et al. 2014; Bernier et al. 2011; Betts et al. 2014, 2019; Colditz et al. 2012, 2014; Fontana et al. 2010; Hanesiak et al. 2011; Ji et al. 2010; Liu et al. 2020; Talbot and Meades 2011; Trishchenko et al. 2009, 2016*b*; Trishchenko and Wang 2018; Trishchenko and Ungureanu 2021; Way and Lewkowicz 2016). The CCRS MODIS processing system has also been successfully applied to lake water quality and algal bloom mapping (El-Alem et al. 2012, 2014, 2019; Ratté-Fortin et al. 2018, 2020), lake ice mapping (Gignac et al. 2017), and some other applications.

An important high-level product derived from the CCRS MODIS time series is the melting season (April–September) snow/ice probability maps designed to study the annual dynamics of Minimum Snow/Ice (MSI) extent (Trishchenko et al. 2016*b*; Trishchenko 2020; Trishchenko and Ungureanu 2021). These time series are available at 250 m spatial resolution since 2000 for two regions: (1) Canada and neighbouring landmass, 5700 km × 4800 km; and (2) the Northern Circumpolar area, 9000 km × 9000 km. Trishchenko and Wang (2018) demonstrated that MSI extent variations over the Canadian Arctic region derived from CCRS warm season snow/ice probability maps are very well correlated to variations in the local climate dynamics, such as warm-season average temperature, energy fluxes, and snow cover. Figures 1*a*–1*b* demonstrate that CCRS MODIS composites also have a good potential for LFI mapping in the coastal zone.

We utilized 10-day 250 m MODIS image clear-sky composites produced for the backward and the forward scattering directions and aggregated them to monthly intervals for the LFI identification. The average cloud fraction observed from MODIS and other sources during the spring and early summer period over the coastal areas of the Beaufort Sea is typically below 0.7, i.e., 70% (Jin et al. 2007; Platnick et al. 2015; Wang and Key 2005). As such, there is a sufficient number of clear-sky pixels (∼30%) each month to observe the landfast sea ice over this region in our images. This value compares favourably with the average global total cloud amount observed from satellites, which is equal to 0.68 (±0.03) (Stubenrauch et al. 2013) and allows the generation of surface-level products from satellite observations on a routine basis (Liu et al. 2017).

The mean (m) and standard deviation (σ) values of spectral reflectances for MODIS bands B1 (red), B2 (near-infrared), B4 (green), and B6 (shortwave infrared) have been computed for each month. The composite maps of the mean reflectances can be utilized for the identification of sea ice, as MODIS bands B1, B2, and B6 have good capability to separate water bodies and snow-free land from snow/ice-covered surfaces. The monthly maps of standard deviations for bands B1, B2, and B4 are used for the identification of variability in spectral reflectances. The areas

Fig. 2. Monthly mean (m) and standard deviation (σ) maps of Moderate Resolution Imaging Spectroradiometer reflectances for April 2016: false-colour images for (*a*) mean reflectances of bands B6, B2, and B1 and (*b*) for standard deviations of reflectances of bands B4, B2, and B1.

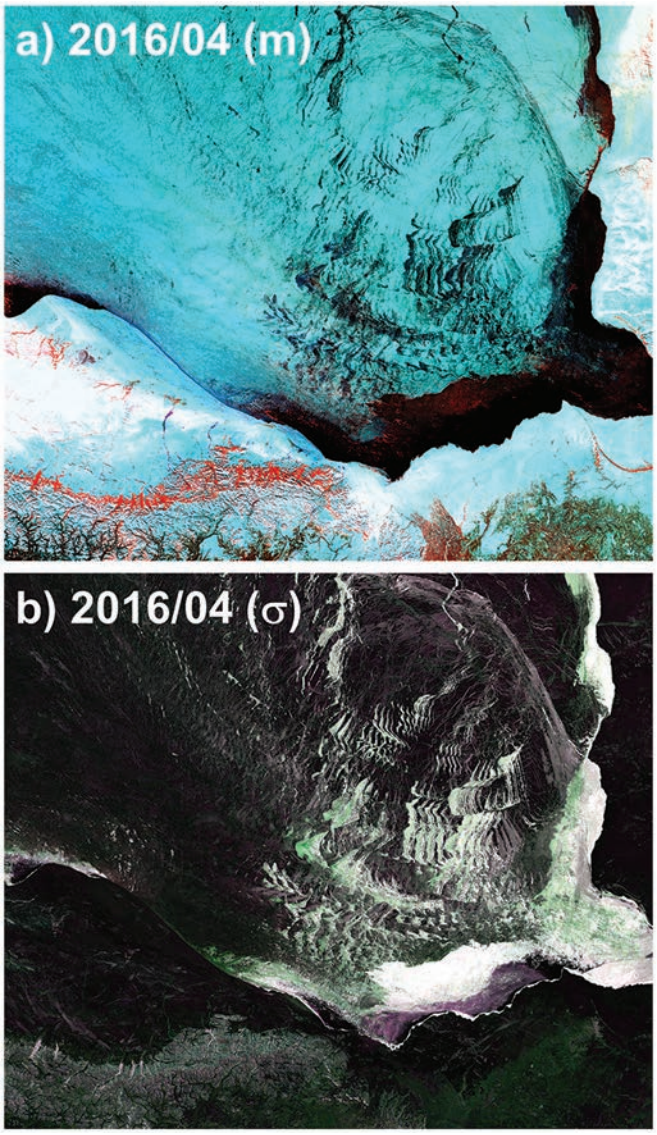

with high σ values indicate unstable sea-ice conditions (i.e., changes between ice and water) because of large differences in spectral reflectances of water and sea ice and snow. The areas with low σ values indicate persistently similar surface reflectance and, therefore, point to stable sea ice or open water conditions. Comparisons of high and low σ values (Fig. 2) for April 2016 show differences in monthly mean reflectances (bands B6, B2, and B1) and standard deviations of reflectances (bands B4, B2, and B1) composed as false-colour RGB images.

Due to inconsistent results from attempted automated classifications, we have mapped the LFI zones manually, employing visual spatial contrasts synchronously observed in two images (m and σ). Dammann et al. (2019) and Meyer et al. (2011) reported similar approach and recommendations. We limited the application of our method for LFI identification to the April–September time frame because the quality of images in solar bands B1–B7 is low in the High Arctic zone during the October–March period. Further details of the LFI delineation method can be found in Trishchenko and Luo (2021). The CCRS LFI data are available (ftp://ftp.ccrs.nrcan.gc.ca/ad/Trishchenko/BeaufortSeaLandfastIce.2000-2019/).

The spatial uncertainty in the delineation of the LFI boundary position using manual mapping is estimated to be ±1 pixel, which is equivalent to ±250 m for our imagery and selected map projection. Due to the random nature of errors coming from the manual delineation, we do not expect any systematic spatial biases in the mapping of the LFI boundary position. An additional potential source of uncertainty in the LFI delineation could be incorrect identification of the boundary line separating the stabilized ice from nonstabilized sea-ice zones in ambiguous cases. In complex situations, we normally select the LFI position that was consistent with the preceding image history and was located closer to the coast. These rules cannot be easily quantified and converted into uncertainty estimates. Comparison with alternative and independent sources of the LFI edge position would be the best approach to evaluate potential uncertainties in the LFI spatial extent. It constitutes one of the objectives of this study.

CIS charts

The CIS charts in ArcInfo E00 format were obtained from the CIS archive (https://iceweb1.cis.ec.gc.ca/Archive/). These vector data are generated using a map scale of up to 1:400 000, which theoretically could correspond to a raster pixel resolution of about 200 m. The coding of parameters in E00 files follows recommendations of the Sea Ice Geo-Referenced Information and Data standard (JCOMM 2014). For mapping the LFI, we utilized the "form of ice" (F) codes. The LFI is coded by value 8 in any of the form of ice fields FA, FB, FC, etc. This method is different from the one chosen by Galley et al. (2012), who utilized the "ice concentration" (C) codes CT, CA, and CB, etc. There are no official recommendations in the Sea Ice Geo-Referenced Information and Data to link the LFI and the ice concentration, although the LFI is normally associated with the highest ice concentration 10/10th (i.e., 100%).

ArcInfo vector files were converted into raster data on a 250 m spatial grid in map projection compatible with the CCRS MODIS clear-sky composites using the FORTRAN-90 code developed in this project. Most of the CIS data files for the 2000–2019 period are available at weekly temporal resolution. Before 2008, some data for the January–April period were available at monthly or bi-weekly intervals. Weekly CIS ice charts over the Beaufort Sea study region were rasterized with four classes: (1) open water, (2) LFI, (3) ice in any concentration, form, and age, and (4) land (Fig. 3). Time series of raster files have been produced from January 2000 to December 2019. Because of uneven temporal spacing (weekly, semi-monthly, and monthly) of the CIS data, we replicated the low-frequency data points to a weekly temporal resolution when computing monthly and seasonal statistics. This procedure ensures the proper weighting of observations and reduces possible biases due to unequal sampling.

Bathymetry and ERA5 temperature

Bathymetry data were required to obtain information about the water depth at the edge of the LFI zone. There is a correspondence between the average seaward LFI edge location and the 20 m isobaths reported for some parts of the Beaufort Sea (Mahoney et al. 2014; Trishchenko and Luo 2021), but a relationship between water depth and location of the LFI edge has not been analyzed yet for the entire Beaufort Sea region.

We used the general bathymetric chart of the oceans (GEBCO Bathymetric Compilation Group 2020) for bathymetry of the ocean floor and land surface topography from the British Oceanographic Data Center (https://www.bodc.ac.uk). Image tiles were extracted and re-projected from geographic into Lambert Conformal Conic (LCC) projection at 250 m spatial resolution and merged over the study region (Fig. 1*c*).

Fig. 3. Weekly Canadian Ice Service ice charts over the Beaufort Sea study region for April 2016. Figures 3*a*–3*d* show ice conditions with four classes: (1) open water; (2) landfast ice; (3) ice in any concentration, form, and age; and (4) land.

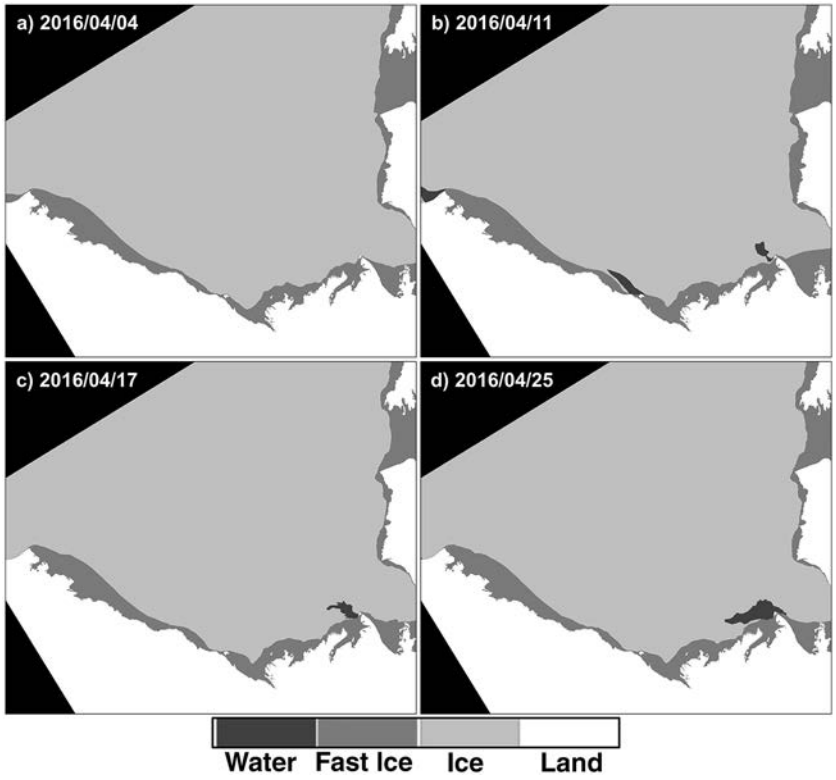

We utilized the monthly mean surface air temperature fields at 2 m height (T2m) produced by the European Centre for Medium-Range Weather Forecasts in the framework of the latest climate reanalysis ERA5 (Copernicus Climate Change Service (C3S) 2020; Hersbach et al. 2020) to study a possible correlation between time series of the LFI spatial extent and climate conditions. The ERA5 T2m data set with a spatial resolution of 0.25° × 0.25° were remapped at 250 m spatial resolution into the LCC map projection using a bilinear resampling scheme as described by Trishchenko (2019). Linear trends of mean temperature for the January–May, the April–June, and the annual time series over the period of 2000–2019 were computed for a joint analysis with the LFI data showing positive trends over the whole region since 2000 (Fig. 4). Regions 1–4 along the southern coastal zone have the highest T2m increase rates. The largest annual trends have been detected over the Mackenzie Bay area where the annual mean rate is about 2 K/decade and can be even larger during the January–May season.

Derived parameters

For all of the Beaufort Sea subregions, we have estimated the following parameters: (1) the LFI spatial extent, (2) the distance of outer seaward LFI edge from the coast, (3) the water depth at the outer seaward LFI edge, (4) the date of LFI onset, (5) the date of LFI break-up, (6) the length of the ice-free period (as a conjugate parameter to the LFI duration period). The timing parameters (4–6) have been derived from the CIS time series, as the CCRS monthly data have no sufficient temporal resolution for this purpose. We utilized the threshold area of 0 km^2 for the total LFI extent (S) over the entire subregion to determine the onset and break-up dates (i.e., S = 0 km^2). This approach differs from the one implemented by Galley et al. (2012), who determined the onset and break-up dates for each grid cell 2 km × 2 km and then aggregated results over a specific study region. For each subregion, we displayed time series of the above parameters with an original temporal resolution, multi-annual time series of January–May mean values (winter season as defined by Yu et al. 2014) and April–June mean values (spring season as defined by Trishchenko and Luo (2021) for comparison between the CIS and the CCRS results), as well as their seasonal cycle (monthly mean values).

Results

Region 1: Alaska coast

The CCRS and CIS time series of spatial LFI extent for Region 1: Alaska coast (Figs. 5*a*–5*c*) show a generally high degree of consistency with a correlation coefficient of about 0.65 (Fig. 5*b*). There is higher variability in the CIS results relative to the CCRS time series (Fig. 5*a*), which can be attributed to the higher temporal frequency of the CIS data (weekly CIS versus monthly CCRS maps), as well as to the different length of data collection interval (1 day in CIS ice chart versus 1 month in CCRS method). A much shorter data collection period may lead to the possible inclusion of non-stabilized ice with high concentration at the outer ice edge into the landfast category because the ice stability cannot always be reliably determined using the data collected on a specific date. The monthly aggregated interval employed in the CCRS LFI retrievals provides better discrimination of stabilized versus non-stabilized sea ice based on monthly statistics of reflectance. As a consequence, the CCRS LFI maps systematically underestimate the area relative to the CIS results (on average by ∼7.2% for Region 1, see Table 1).

The linear trend for the CIS winter spatial extent is small and positive: 0.58 (±1.41) × 10^3 km^2/decade (Table 2). Trends for the spring spatial extent are small and negative: −0.45 (±1.22) × 10^3 km^2/decade (CIS) and −0.57 (±1.01) × 10^3 km^2/decade (CCSR). All trends for Region 1 in Table 2 are not statistically significant, which is in general agreement with Mahoney et al.'s (2014) conclusion for the 1996–2008 period.

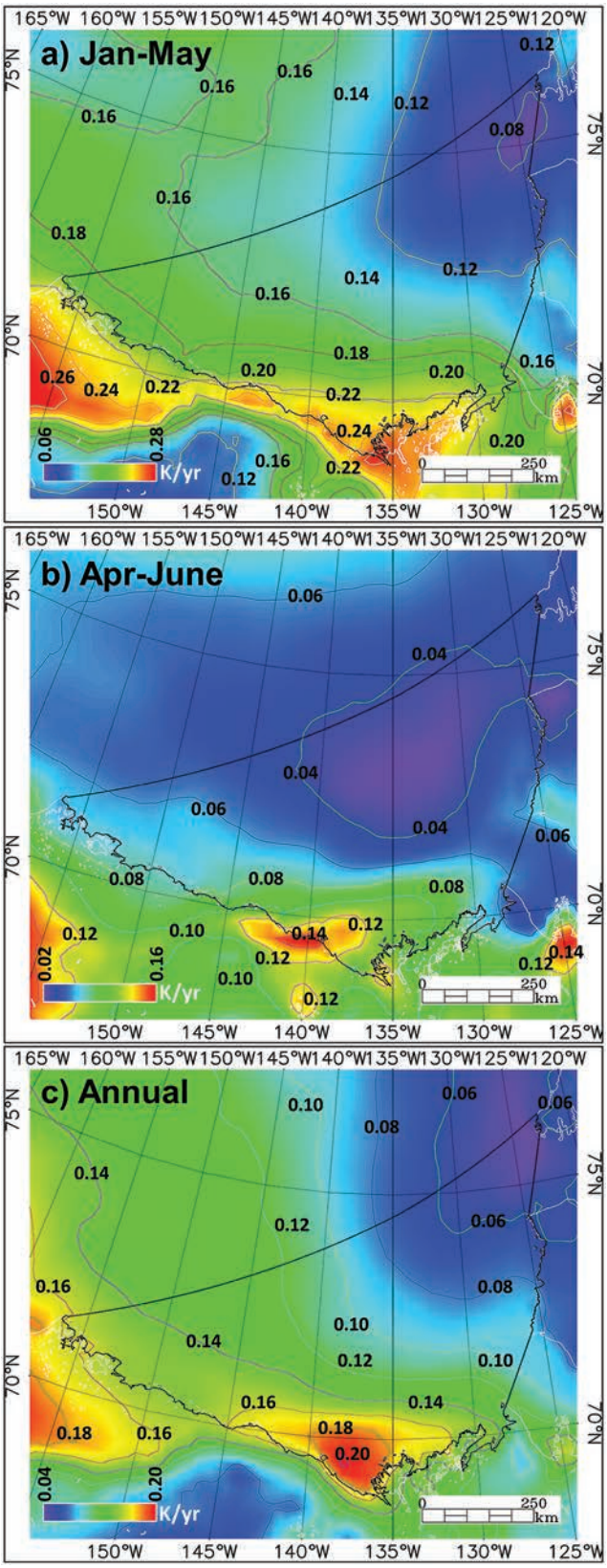

Fig. 4. Maps of linear trends in the ERA5 surface air temperature T2m (K/year) over the Beaufort Sea region for 2000–2019. (*a*) January–May average; (*b*) April–June average; (*c*) annual mean. The ERA5 data were acquired from the European Copernicus data archive (C3S 2020; Hersbach et al. 2020).

Despite the good general agreement between the CIS and the CCRS results, a few outliers were observed in the spring of 2009, 2010, and 2019. An example of this comes from the April 2009 data set (Fig. 6), which shows large variability in the weekly extents of the CIS LFI zones for Regions 1–3 and the western part of Region 4. The CIS LFI area for 27 April 2009 is the smallest among the three charts. The area for 20 April 2009, is the largest one. Because the CCRS method uses monthly variability to determine stable areas corresponding to low values of standard deviations, it maps the minimum envelope, i.e., infimum, of LFI spatial extent for that month. It is clear that although the CIS operational ice product provided an adequate identification of the landfast zone for each date, on a monthly time scale, the large LFI areas displayed in violet–purple shades in Figs. 6*a*–6*b* correspond to nonstabilized fractured ice identified using the CCRS monthly composite images (Figs. 6*c*–6*d*).

The agreement between the CCRS and the CIS results for the average water depth at the outer seaward LFI edge (Figs. 5*e*, 5*f*, 5*g*) is good with an average correlation coefficient of 0.61 (Fig. 5*f*) and the average difference in spring equal to 7.74 m (CIS: −38.24 m versus CCRS: −30.5 m; Table 3). The main reason for the CCRS–CIS bias stems from the fact that the CIS characterize the ice as landfast further toward the outer seaward edge. In Region 1, the ocean depth increases sharply converting small differences in the CCRS and the CIS positions of LFI outer edge into large differences in the associated water depth.

The average distances of the outer seaward LFI edge from the coast (Figs. 5*i*–5*k*) demonstrate general agreement between the CCRS and the CIS data with correlation coefficient for the spring months equal to 0.65 (Fig. 5*j*). The average difference is 2.81 km or 10.2% (CIS: 27.66 km versus CCRS: 24.85 km; Table 4). Comparison of the annual cycle of all three parameters (spatial extent, ocean depth, and distance from coast) clearly shows underestimation of CCRS results for the outer LFI edge position relative to the CIS data (Fig. 5).

The timing of spring LFI break-up, autumn LFI onset, and duration of LFI-free season and their long-term trends over the 2000–2019 period for Region 1 (Alaska) show the later onset, the earlier break-up, and the longer ice-free period (Fig. 7). However, all these trends are not statistically significant.

Region 2: Barter Island – Hershel Island

Region 2 has the smallest area among all regions. The multiannual mean distribution of sea-ice probability (Fig. 1*b*) shows that this region belongs to a transition zone where the coastal LFI properties are not easily separated from the mobile ice zone at least over its western part. The characteristic feature of this region is the very narrow zone of 30 m isobath (Figs. 1*b*, 1*c*) that embraces most of LFI extent in the Beaufort Sea region. Figures 8*a*–8*c* display time series of the LFI spatial extent for Region 2 (Barter – Hershel). The overall agreement between the CIS and the CCRS results is reasonable, but not as good as for other subregions. The difference in the spring LFI extent is 0.42 $\times$ 10^3 km^2 (2.32 $\times$ 10^3 km^2 from CIS versus 1.90 $\times$ 10^3 km^2 from CCRS) or 18.1%. The correlation coefficient is 0.20 (Fig. 8*b*). The CIS time series contain a significant number of outliers. Close analysis shows that the main reason for differences between the CCRS and the CIS LFI delineation relates to the characterization of ice at the outer edge which is similar to discrepancies found in Region 1 (Alaska). The long-term trends of the LFI spatial extent in Region 2 are negligible and statistically not significant (Table 2).

Results for the water depth at the outer seaward LFI edge are shown in Figs. 8*e*–8*g*. The level of agreement between the CIS and the CCRS results reflects the situation for their LFI spatial extent. The difference for the April–June depth is equal to 10.98 m (−32.48 m for the CIS data and −21.50 m for the CCRS data). This difference is 33.8% relative to the CIS value. The big difference is mainly driven by a very large outlier described earlier for April 2009,

Fig. 5. Time series of the landfast ice (LFI) parameters for Region 1: Alaska: (*a*–*d*) the total spatial extent; (*e*–*h*) the mean ocean depth at the LFI edge; (*i*–*l*) the mean distance of LFI edge from the coast.

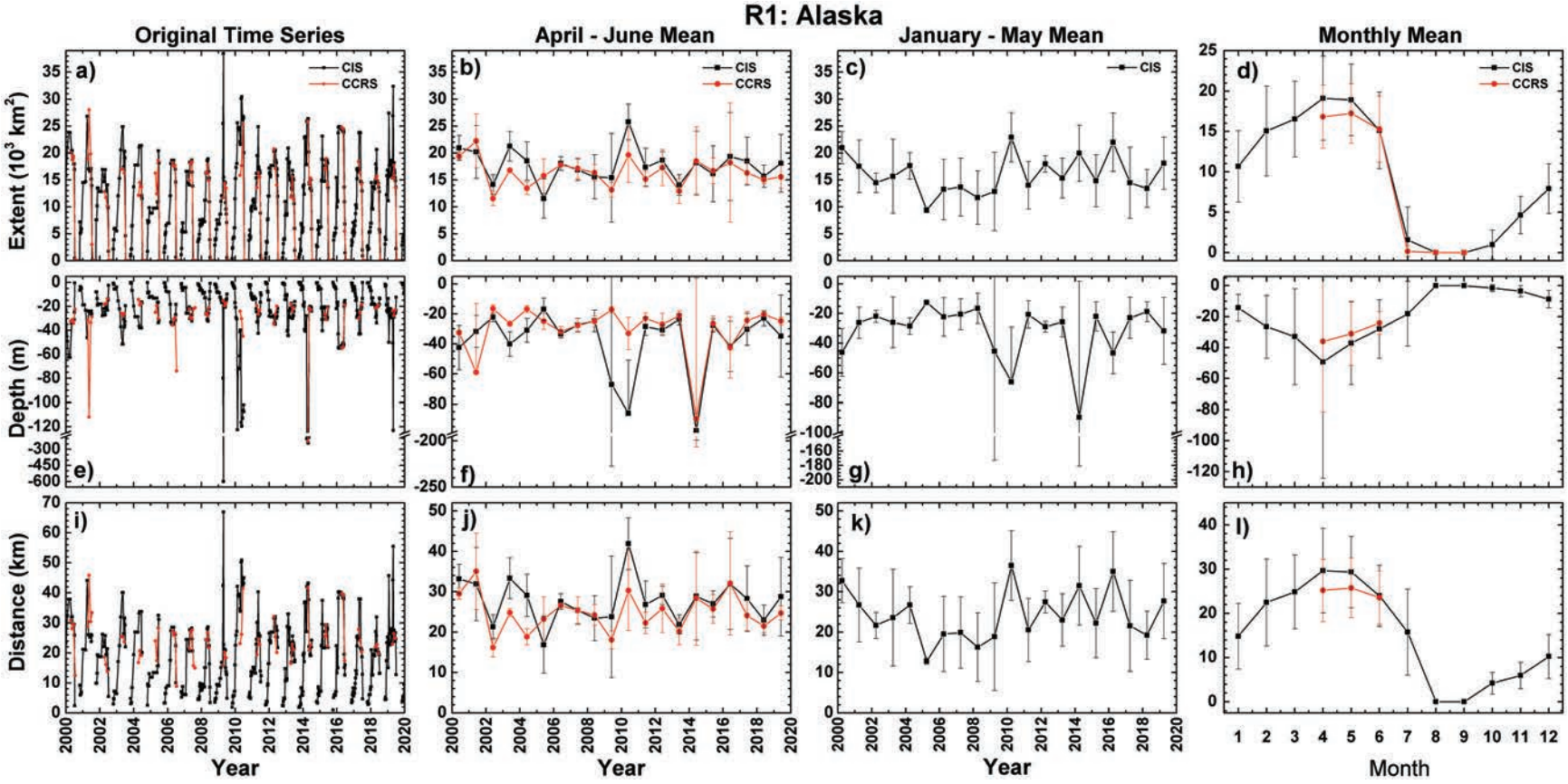

Table 1. Monthly, seasonal, and annual mean values of the total landfast ice (LFI) area (10^3 km^2) derived from the Canadian Ice Service (CIS) and the Canada Centre for Remote Sensing (CCRS) data for 2000–2019.

	Region 1: Alaska		Region 2: Barter–Hershel		Region 3: Mackenzie Bay		Region 4: Richards–Bathurst		Beaufort Sea entire region	
Month	CIS	CCRS	CIS	CCRS	CIS	CCRS	CIS	CCRS	CIS	CCRS
1	10.66	—	1.24	—	7.64	—	9.66	—	33.71	—
2	15.05	—	1.49	—	8.68	—	11.48	—	42.59	—
3	16.52	—	1.88	—	9.77	—	12.95	—	47.39	—
4	19.09	16.83	2.80	1.94	10.99	10.00	13.76	13.15	53.43	47.67
5	18.91	17.23	2.41	2.14	10.87	10.11	14.14	13.67	52.66	49.14
6	15.12	15.27	1.76	1.63	5.65	5.35	10.85	10.53	39.25	38.51
7	1.56	0.16	0.10	0.01	0.15	0.03	0.45	0	5.01	4.32
8	0	0	0	0	0	0	0	0	0.47	2.22
9	0	0	0	0	0	0	0	0	0.42	0.92
10	0.97	—	0.05	—	0.46	—	0.49	—	3.54	—
11	4.65	—	0.47	—	4.10	—	3.93	—	16.00	—
12	7.91	—	0.71	—	5.89	—	7.81	—	26.14	—
1–5	16.05	—	1.96	—	9.59	—	12.40	—	45.95	—
4–6	17.71	16.44	2.32	1.90	9.17	8.49	12.92	12.45	48.44	45.11
1–12	9.20	—	1.08	—	5.35	—	7.13	—	26.72	—

Note: "—" denotes no data available from CCRS retrievals due to solar zenith angle limitations.

Table 2. The long-term linear trends (10^3 km^2/decade) and their uncertainty for landfast ice (LFI) spatial extent over the 2000–2019 period.

		Season	
Region		Winter (January–May)	Spring (April–June)
1: Alaska	CIS	0.58 ± 1.41 (0.69)	–0.45 ± 1.22 (0.72)
	CCRS	—	–0.57 ± 1.01 (0.58)
2: Barter–Hershel	CIS	0.21 ± 0.25 (0.42)	0.00 ± 0.25 (0.99)
	CCRS	—	–0.08 ± 0.20 (0.69)
3: Mackenzie Bay	CIS	–0.73 ± 0.57 (0.22)	**–1.68 ± 0.60 (0.01)**
	CCRS	—	**–1.88 ± 0.79 (0.03)**
4: Richards–Bathurst	CIS	–0.95 ± 0.59 (0.12)	**–2.12 ± 0.83 (0.02)**
	CCRS	—	**–2.06 ± 0.96 (0.05)**
Beaufort Sea	CIS	–1.03 ± 1.66 (0.54)	**–4.45 ± 1.69 (0.02)**
	CCRS	—	**–4.73 ± 2.17 (0.04)**

Note: Statistical significance (p = Prob>|t| or p value) is shown in parentheses. Numbers in boldface type indicate statistically significant trends at $p \leq 0.05$. "—" denotes no data available from CCRS retrievals. CIS, Canadian Ice Service; CCRS, Canada Centre for Remote Sensing.

and also by a significant outlier observed in 2019. The correlation coefficient (largely affected by these two outliers) between the CCRS and the CIS spring data are −0.24 (Fig. 8*f*). Except for these two cases, the variations of CCRS and CIS data follow each other closely in the −20 to −30 m depth range. Two outliers identified in 2009 and 2019 are not only the outliers in terms of large differences between the CCRS and the CIS data, but these outliers are also large anomalies relative to the Region 2 bulk CIS results, which vary mostly within a depth range from −20 to −30 m.

Figures 8*i*–8*k* show the average distance of the outer seaward LFI edge from the coast for Region 2. The level of agreement is reasonable and reflects the situation described for the LFI spatial extent. The correlation coefficient is equal to 0.19 (Fig. 8*j*). The absolute difference is 2.37 km (11.31 km from CIS versus 8.94 km from CCRS) or 21% relative to the average CIS distance in spring.

The seasonal cycle (monthly mean values) of all three parameters for Region 2 (Figs. 8*d*, 8*h*, 8*l* and Tables 1, 3, 4) are in reasonable agreement except multi-annual monthly mean CIS values for April that are not consistent with the rest of the CIS and CCRS data. The trends in LFI break-up and onset dates and length of the ice-free period agree with general warming trends, i.e., earlier break-up, later onset, and longer ice-free interval, although these trends are not statistically significant (Fig. 7*b*).

Region 3: Mackenzie Bay

Region 3 has two interesting features of LFI extent: (1) contours of increased sea ice presence follow closely the shape of the 20 m isobath; (2) there is a noticeable area of reduced sea-ice presence along the boundary of the Mackenzie River delta (Fig. 1*b*). The first feature is consistent with findings reported by Trishchenko and Luo (2021) for Banks Island LFI properties and the conclusion of Mahoney et al. (2014) for the western part of the Beaufort Sea. The second feature is associated with the role of large freshwater discharge from the Mackenzie River in spring break-up and its effect on the LFI melting because the Mackenzie River can transport an enormous amount of heat across immense continental watersheds into the Arctic Ocean (Nghiem et al. 2014). The agreement between the CCRS and the CIS data are generally very good for this region (Fig. 9*a*). The difference in the LFI spatial extent for the spring season (April–June) is 0.68 × 10^3 km^2 (9.17 × 10^3 km^2 from CIS data and 8.49 × 10^3 km^2 from CCRS data) or 7.4% relative to CIS value. The correlation coefficient between the CIS and the CCRS data for the spring is 0.84 despite a few outliers including the one already described for April 2009 (Fig. 9*b*). The multi-annual linear trends (Fig. 9*b*) show a statistically significant decrease in the spring LFI area for both sources: CIS and CCRS. The linear trends for the springtime series are −1.68 (±0.60) × 10^3 km^2/decade (p = 0.01)

Fig. 6. Canadian Ice Service (CIS) and Canada Centre for Remote Sensing (CCSR) Moderate Resolution Imaging Spectroradiometer (MODIS) data for April 2009: (*a*) CIS ice charts for 13 April, 20 April, and 27 April combined in one RGB image for the entire Beaufort Sea region; (*b*) subset of (*a*) showing a zoom for the selected rectangular area; subset (*c*–*d*) false-colour image of CCRS MODIS monthly mean (m) and standard deviation (σ) of reflectances for the subset in Fig. 6*b*. The green curve marks the CCRS landfast ice (LFI) delineation for April, which closely resembles the minimum LFI area in combined CIS results.

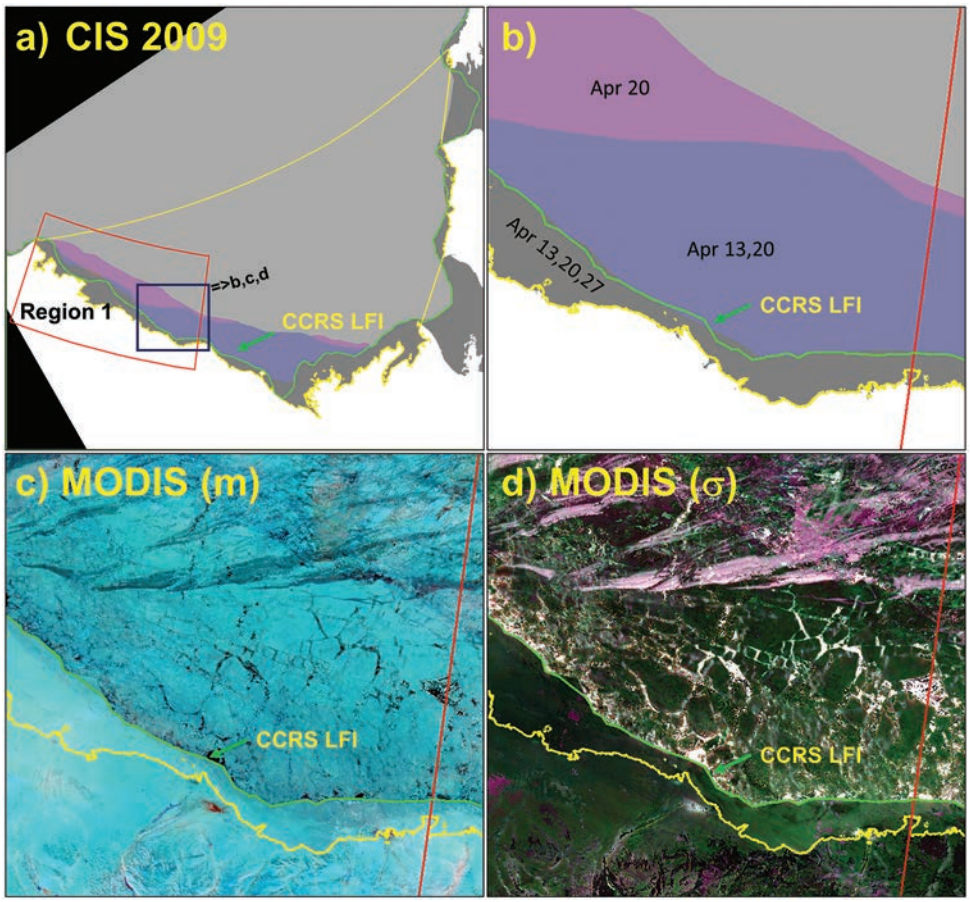

for the CIS data and $-1.88\ (\pm 0.79) \times 10^3$ km^2/decade ($p = 0.03$) for the CCRS data. The linear trend for the winter period is less significant: $-0.73\ (\pm 0.57) \times 10^3$ km^2/decade ($p = 0.22$). The April–June LFI spatial extent shows a strong and statistically significant negative correlation with the ERA5 T2m temperature time series for the Mackenzie Bay area which is consistent with physics describing the impact of the warming environment on the cryosphere. The correlation coefficient between the CCRS and ERA5 time series is −0.45 (p = 0.048) and −0.66 (p = 0.001) between the CIS and ERA5 time series.

The CIS and CCRS comparison of the water depth at the outer seaward LFI edge shows a difference for the April–June mean values of 8.00 m (−33.26 m from CIS data and −25.26 m from CCRS data) or 24% (Fig. 9). The correlation coefficient is 0.22 (Fig. 9*f*), however, if the outliers for 2009 were removed, the correlation would increase to 0.80.

The CIS and CCRS time series with original temporal resolution show good general agreement to the calculated average distance to the seaward edge (Figs. 9*i*–9*k*) with only a few significant outliers (observed in April 2009, and on 30 January 2012). These one-point anomalies had a very significant impact on all three analyzed LFI parameters. The January anomaly had no effect on the CIS–CCRS comparison conducted for April–June data. The difference between the CIS and the CCRS mean values of the average outer seaward LFI edge distance from the coast is 2.74 km (28.76 km from CIS data and 26.02 km from CCRS data) or 9.5%. The correlation coefficient for the April–June time series is 0.79 (Fig. 9*j*). The impact of these two outliers is observed as large standard deviations for winter seasons 2009 and 2012 as shown in Fig. 9*k*.

Analysis of the seasonal cycle and monthly mean standard deviations can serve as a good consistency check for the quality of input data. This is shown in Figs. 9*d*, 9*h*, and 9*l* and in Tables 1, 3, and 4. Large standard deviations of the CIS values for all three parameters (extent, depth, and distance) for January and April may indicate possible inconsistences with LFI delineation in the CIS data. Large standard deviations in June are expected due to intensive melt and rapid decrease of LFI cover during this period.

Trends in the break-up and onset dates and duration of the ice-free season for Region 3 (Mackenzie Bay) reveal no evident trend in the timing of freeze-up onset (Fig. 7*c*). It shows only a minor indication of earlier start: −0.11 (±0.30) day/year with p = 0.72 (i.e., not statistically significant). However, there is a statistically significant signal of an earlier break-up: −0.76 (±0.26) day/year (p = 0.01). The combination of these two trends leads to a noticeable increase in the duration of the ice–free season for the Mackenzie Bay region by 0.64 (±0.47) day/year, although this is not very significant in the statistical sense (p = 0.19).

Region 4: Richards Island – Cape Bathurst

The Region 4 time series of the LFI spatial extent from the CIS and the CCRS show a high level of agreement (Figs. 10*a*–10*c*). Only one noticeable outlier can be seen for January 2012 in the CIS

Table 3. Monthly, seasonal, and annual mean values of the average ocean depth (m) at the outer seaward landfast ice (LFI) edge derived from the Canadian Ice Service (CIS) and the Canada Centre for Remote Sensing (CCRS) data over the 2000–2019 period.

	Region 1: Alaska		Region 2: Barter–Hershel		Region 3: Mackenzie Bay		Region 4: Richards–Bathurst	
Month	CIS	CCRS	CIS	CCRS	CIS	CCRS	CIS	CCRS
1	–14.28	—	–18.19	—	–24.51	—	–12.18	—
2	–26.63	—	–18.12	—	–22.99	—	–16.12	—
3	–32.97	—	–21.06	—	–27.27	—	–19.48	—
4	–49.43	–36.11	–50.92	–21.48	–44.72	–28.53	–21.49	–19.43
5	–37.24	–31.16	–25.30	–23.18	–35.52	–28.45	–22.28	–20.54
6	–28.06	–24.22	–21.21	–19.85	–19.54	–18.78	–17.90	–15.73
7	–18.19	—	–16.73	–12.09	–7.49	—	–9.58	—
8	—	—	—	—	—	—	—	—
9	—	—	—	—	—	—	—	—
10	–1.54	—	–2.42	—	–1.50	—	–1.67	—
11	–3.54	—	–7.19	—	–5.51	—	–4.14	—
12	–8.72	—	–10.60	—	–10.76	—	–9.36	—
1–5	–32.11	—	–26.72	—	–31.00	—	–18.31	—
4–6	–38.24	–30.50	–32.48	–21.50	–33.26	–25.26	–20.56	–18.57
1–12	–22.06	—	–19.18	—	–19.98	—	–13.42	—

Note: "—" denotes no data available. Data are not available due to lack of retrievals. For CCRS data, this occurs due to lack of valid observations and (or) ice-free conditions during the warm season. For CIS data, this occurs due to ice-free conditions during the warm season. Under the ice-free conditions, all LFI parameters, except spatial area/extent, are not defined.

Table 4. Monthly, seasonal, and annual mean values for the average distance (km) of the outer seaward landfast ice (LFI) edge from the coast derived from the Canadian Ice Service (CIS) and the Canada Centre for Remote Sensing (CCRS) data over the 2000–2019 period.

	Region 1: Alaska		Region 2: Barter–Hershel		Region 3: Mackenzie Bay		Region 4: Richards–Bathurst	
Month	CIS	CCRS	CIS	CCRS	CIS	CCRS	CIS	CCRS
1	14.83	—	5.98	—	20.17	—	17.63	—
2	22.47	—	6.80	—	23.35	—	22.83	—
3	24.87	—	8.72	—	27.73	—	27.14	—
4	29.68	25.19	13.45	8.74	31.82	26.90	30.06	27.06
5	29.35	25.77	11.45	9.85	31.10	27.88	31.12	28.54
6	23.96	23.59	9.02	8.23	23.37	23.27	25.12	22.42
7	15.76	—	6.62	—	11.82	—	12.99	—
8	—	—	—	—	—	—	—	—
9	—	—	—	—	—	—	—	—
10	4.22	—	1.97	—	4.96	—	3.00	—
11	5.95	—	2.91	—	9.73	—	5.77	—
12	10.24	—	3.81	—	14.29	—	12.99	—
1–5	24.24	—	9.28	—	26.84	—	25.76	—
4–6	27.66	24.85	11.31	8.94	28.76	26.02	28.77	26.01
1–12	18.13	—	7.07	—	19.84	—	18.87	—

Note: "—" denotes no data available. Data are not available due to lack of retrievals. For CCRS data, this occurs due to lack of valid observations and (or) ice-free conditions during the warm season. For CIS data, this occurs due to ice-free conditions during the warm season. Under the ice-free conditions, all LFI parameters, except spatial area/extent, are not defined.

data with no impact on comparison between the CIS and the CCRS springtime series. A very high degree of correlation (0.93) exists between the CIS and CCRS time series for the April–June season (Fig. 10*b*). The average difference between the CIS and the CCRS mean values of LFI spatial extent is 0.47×10^3 km^2 (12.92×10^3 km^2 from the CIS data and 12.45×10^3 km^2 from the CCRS data) or 3.6% relative to the CIS LFI mean. Both data sources demonstrate statistically significant negative trends for the April–June period: -2.12 (± 0.83) $\times 10^3$ km^2/decade with $p = 0.02$ for the CIS LFI spatial extent and -2.06 (± 0.96) $\times 10^3$ km^2/decade with $p = 0.05$ for the CCRS LFI spatial extent (shown as dashed lines in Fig. 10*b*). Together with Region 3 (Mackenzie Bay), this region contributes toward statistically significant negative trends in the April–June LFI spatial extent for the entire Beaufort Sea. The LFI spatial extent for Region 4 shows a strong correlation with the ERA5 T2m temperatures. The correlation coefficient between the April–June CIS and the ERA5 T2m time series over the 2000–2019 period is -0.62 ($p = 0.003$). The correlation between the CCRS and the ERA5 April–June time series is -0.51 ($p = 0.02$). The correlation between the CIS LFI extent for the winter period (January–May) and the ERA5 is -0.37 and less statistically significant than the other two ($p = 0.11$).

Comparison of the average water depth at the outer seaward LFI edge shows a high degree of consistency between the two products (Figs. 10*e*–10*g*). Time series from the CIS and the CCRS sources demonstrate a high degree of consistency with a correlation coefficient equal to 0.93 ($p = 3.98 \times 10^{-9}$) (Fig. 10*f*) and the value of average difference equal to 1.99 m (-20.56 m from CIS

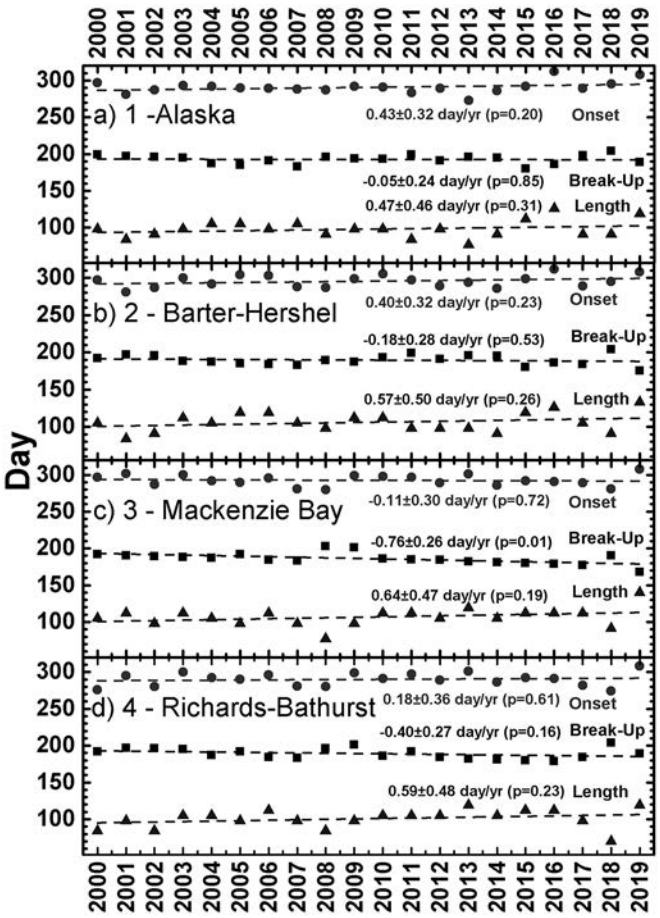

Fig. 7. Trends in break-up (squares) and onset (circles) dates and duration of the ice-free season (triangles). Lines denote the linear trends. Numbers show the absolute values (day/year) with errors and statistical significance (p value).

data and −18.57 m from CCRS data). The average water depth varies mostly between 10 and 30 m. The 20 m isobath position is remarkably consistent with increased sea-ice presence in this region, as shown in Fig. 1*b*.

The results for the distance from the coast for the outer seaward LFI edge show a very high level of agreement between the CIS and the CCRS time series (r = 0.93, p = 4.34 × 10^{-9}) for the April–June data (Figs. 10*i*–10*k*). The difference of the April−June mean values is 2.76 km (28.77 km for the CIS data and 26.01 km for the CCRS data) or 9.6% of the CIS average value. There is an overall negative trend in the 2000–2019 time series for the distance, which is consistent with the negative trend for the LFI spatial extent and increase in the surface air temperature as shown in Fig. 4 for the ERA5 T2m.

The seasonal cycle for Region 4 (Figs. 10*d*, 10*h*, 10*l*) does not show any noticeable deviations of from the regular annual cycle pattern. We attribute it to the lack of any significant outliers in the data except the anomaly on 30 January 2012 in the CIS time series. This single anomaly has been averaged out considerably in the monthly means. The LFI spatial extent reaches a maximum during the April–May period (13.76 × 10^3 km^2 and 14.14 × 10^3 km^2 for CIS data versus 13.15 × 10^3 km^2 and 13.67 × 10^3 km^2 for CCRS data). The ocean depth at the outer seaward LFI edge reaches minimum values in the April–May period (−21.49 m and −22.28 m for CIS data and −19.43 m and −20.54 m for CCRS data). The distance from the coast reaches maximum values (30.06 km and 31.12 km for CIS data and 27.06 km and 28.54 km for CCRS data).

The trends in LFI break-up and onset dates as well as the duration of the ice-free period indicate tendencies for the later onset, earlier break-up, and longer ice-free period (Fig. 7*d*); however, none of the results are statistically significant.

Beaufort Sea LFI spatial extent

This section provides the Beaufort Sea region-wide summary for the LFI extent, which can be considered mathematically as an additive parameter. The derivation of region-wide properties related to the water depth at the outer seaward LFI edge, the distance of the outer seaward LFI edge from the coast, and the LFI timing features is not as straightforward as the LFI spatial extent. Zones of stabilized LFI over the Beaufort Sea region are frequently found in the mouth of M'Clure Strait, Amundsen Gulf, and around Prince Patrick Island (Fig. 1). These zones of stabilized ice are located over deep-water areas. Its evolution cycle is different from the LFI in the southern coastal areas and may include multi-year ice. For these reasons, it makes sense to provide the mapping of detailed LFI properties separately for each region, but mixing them together for the entire Beaufort Sea could lead to misrepresentation of LFI properties that are not linear and not additive.

Due to the large size of the region, only the major outliers can be observed in the CIS data, such as those that occurred in January 2009, January 2012, and April 2019 (Figs. 11*a*–11*c*). Despite these anomalies, the overall agreement between the CIS and the CCRS results is very good. The correlation coefficient for April−June LFI spatial extent time series is 0.73 (p = 2.91 × 10^{-4}) (Fig. 11*b*). The mean difference between the CIS and the CCRS average April−June results is 3.33 × 10^3 km^2 (48.44 × 10^3 km^2 from CIS and 45.11 × 10^3 km^2 and CCRS data) or 6.7% relative to CIS mean value. The systematic underestimation seen in the CCRS data with respect to the CIS results happens due to the large difference in sampling intervals used for mapping of ice properties (1 day in the CIS ice chart production and 1 month in the CCRS method). Negative linear trends in the average April–June multi-year time series of the LFI spatial extent for 2000–2019 are statistically significant and are detected in both the CIS and the CCRS data: −4.45 (±1.69) × 10^3 km^2/decade (p = 0.02) and −4.73 (±2.17) × 10^3 km^2/decade (p = 0.04), respectively (Table 2 and Fig. 11*b*). The trend for average LFI spatial extent for January–May is smaller and not statistically significant: −1.03 (±1.66) × 10^3 km^2/decade (p = 0.54).

The mean annual cycle of the LFI spatial extent for the entire Beaufort Sea region (Fig. 11*d*) show peaks occurring in April−May with the average CIS values of 53.43 × 10^3 km^2 and 52.66 × 10^3 km^2, and the CCRS values of 47.67 × 10^3 km^2 and 49.14 × 10^3 km^2, respectively. The annual mean LFI extent over the entire Beaufort Sea region is 26.72 × 10^3 km^2, i.e., it is about half of the maximum value.

Yu et al. (2014) reported the average value of 50.04 × 10^3 km^2 for the January−May season over the 1976–2007 period and a negative trend of −0.39 (±0.16) × 10^3 km^2/year. Projecting their average value with the reported trend leads to the estimate of the 2000–2019 average LFI area equal to 43.02 × 10^3 km^2, which is close (within 5%) to the average value of 45.95 × 10^3 km^2 derived from the CIS data in this study. This is a somewhat surprising finding taking into account that the results of Yu et al. (2014) have been derived from very coarse resolution data (25 km grid cell). Data with such a coarse spatial resolution cannot adequately capture the properties of a phenomenon with typical spatial size (distance from the cost) that ranges from a few kilometres to about 32 km (Table 3). For the additive parameters, such as the areal extent, it is still possible to obtain accurate overall results if coarse spatial resolution data include accurate fractional coverage values within each grid cell. However, the determination of the accurate factional values still requires high-resolution input. Another important fact is that our analysis for the January−May season over 2000–2019 (Table 2) showed a much weaker trend: −0.103 (±0.166) × 10^3 km^2/year, which

Fig. 8. Similar to Fig. 5, but for Region 2: Barter Island to Herschel Island.

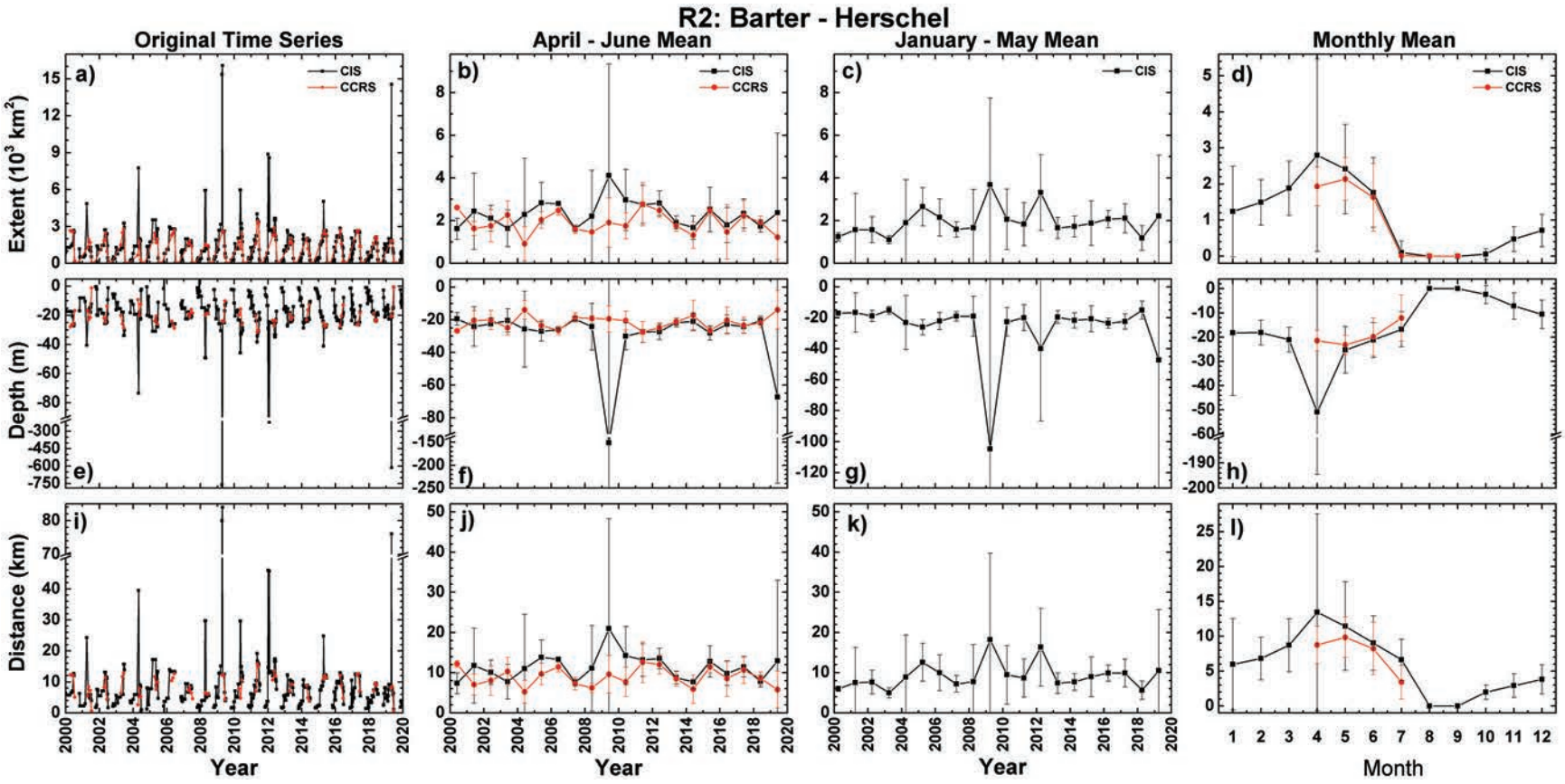

Fig. 9. Similar to Fig. 5, but for Region 3: Mackenzie Bay. Dashed lines show the linear trends.

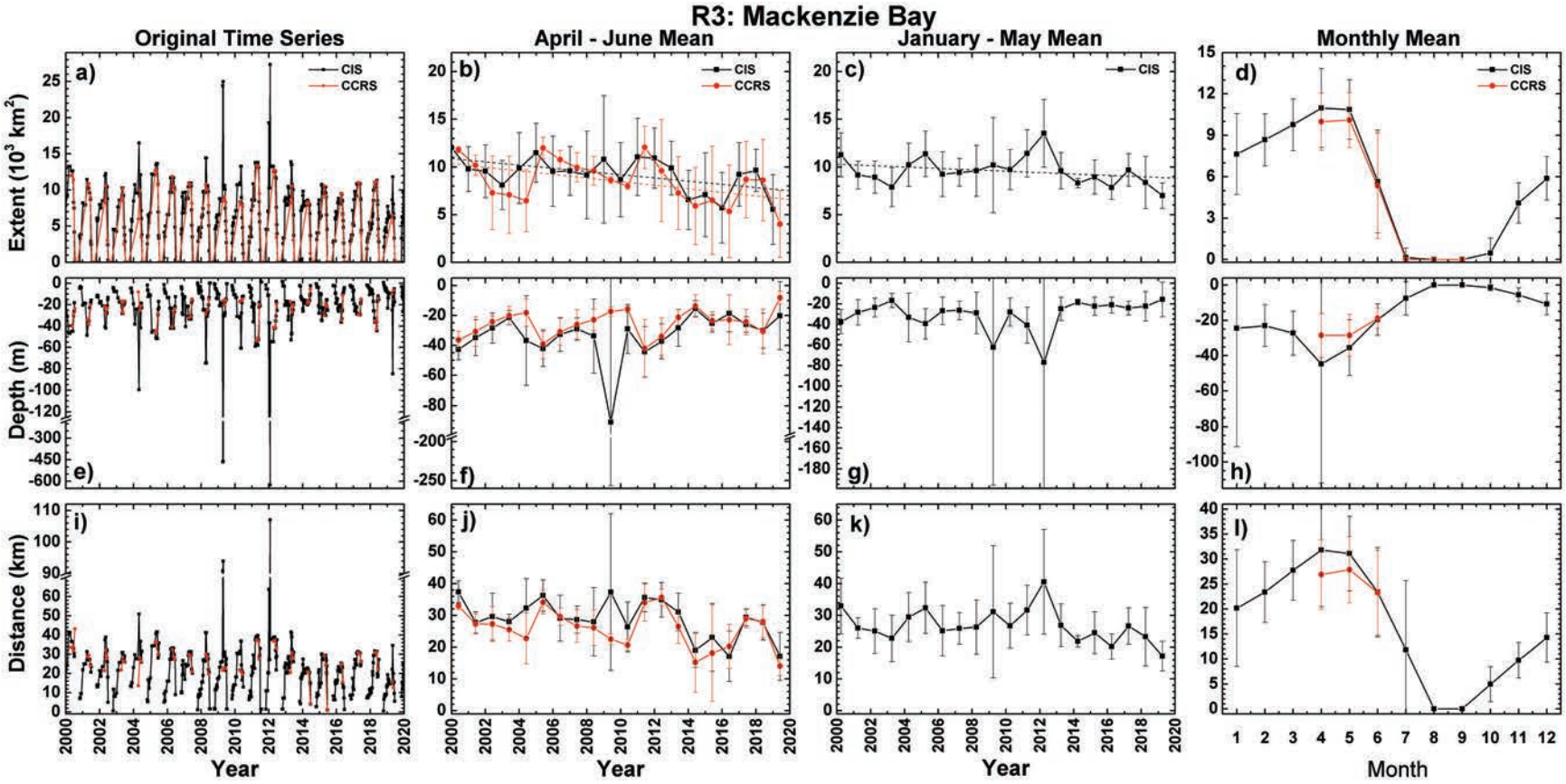

Fig. 10. Similar to Fig. 9, but for Region 4: Richards Island to Cape Bathurst.

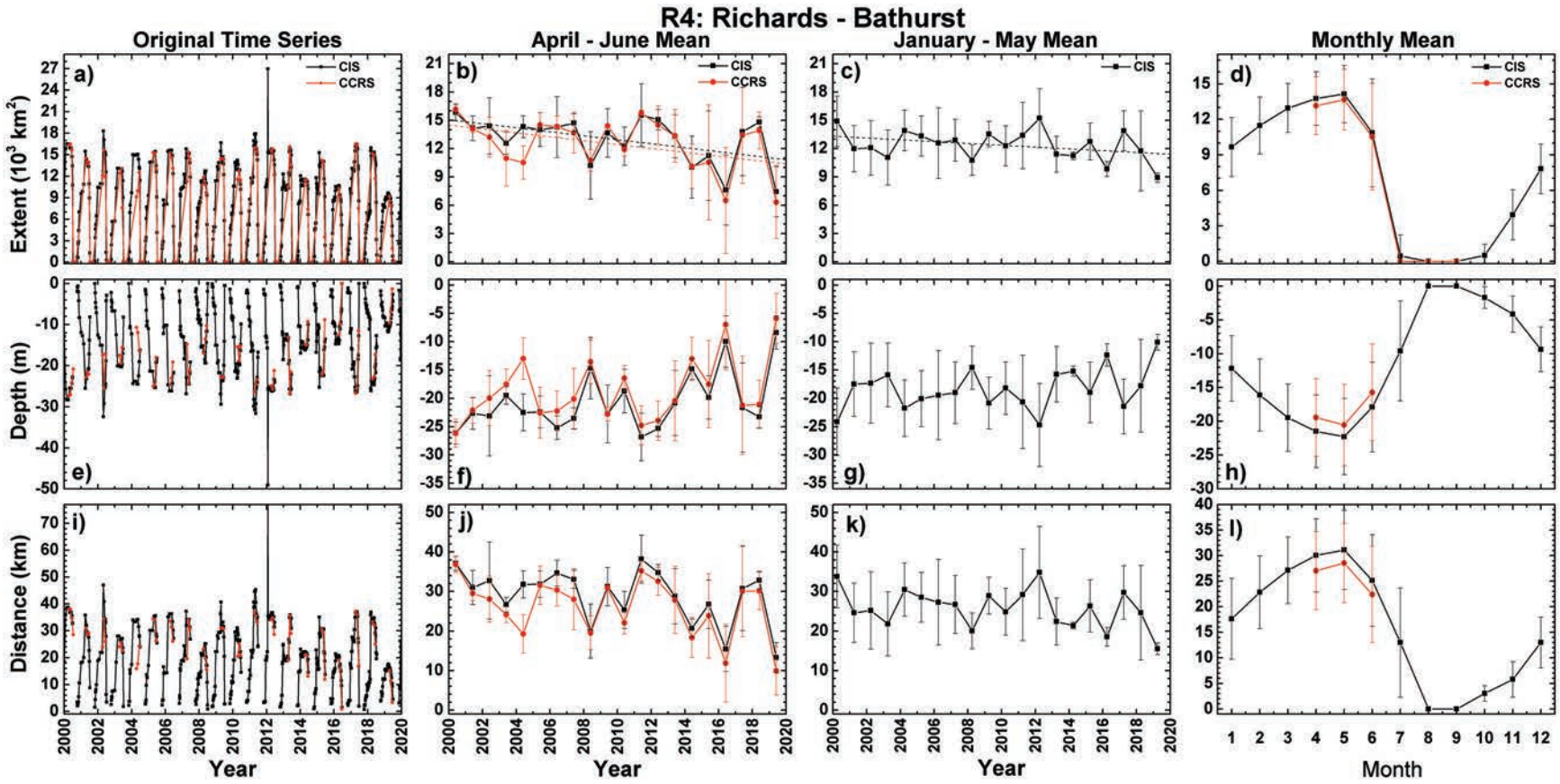

Fig. 11. Time series and monthly mean values of the landfast ice extent for the entire Beaufort Sea region: (*a*) original time series; (*b*) April–June (spring) average values; (*c*) January–May (winter) average values; (*d*) monthly means.

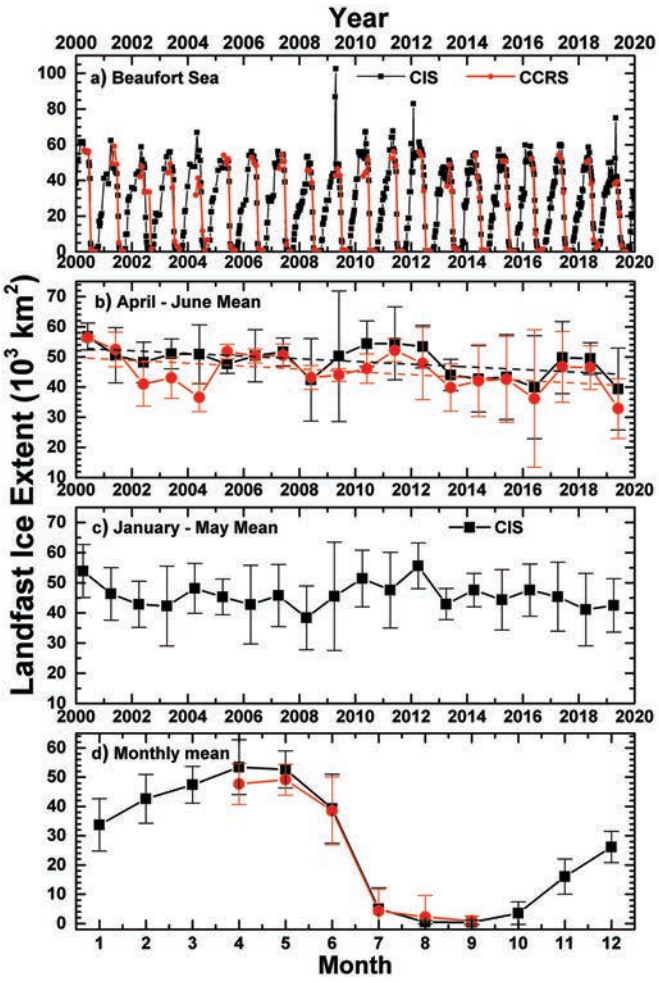

is not statistically significant. As such, it is also possible that close agreement between projected and observed results reported above can be explained by compensation of errors in the absolute values and their trend derived from coarse resolution data. The re-analysis of historical CIS data at their original high spatial resolution could shed more light on this issue.

Dammann et al. (2019) reported the LFI extent (bottomfast, stabilized, and nonstabilized coastal ice) derived from high-resolution SAR imagery over the Beaufort Sea between March and May 2017 equal to 67×10^3 km^2. This included 35×10^3 km^2 of stabilized ice and 2.5×10^3 km^2 of bottomfast ice. The total LFI area (bottomfast and stabilized ice) was, therefore, 37.5×10^3 km^2. Our estimates for the March–May period of 2017 derived from results presented in Fig. 11*a* show the mean LFI spatial extent of 53.35 ($\pm$1.42) $\times 10^3$ km^2 with a maximum of 60.08 $\times 10^3$ km^2, minimum 44.68 $\times 10^3$ km^2, and the median value of 52.10 $\times 10^3$ km^2. The CCRS-derived LFI extent for April–May 2017 is equal to 53.41×10^3 km^2, which is close to the CIS mean value for March–May. This comparison shows that Dammann et al. (2019) estimates of the LFI extent from SAR are generally lower than ours by about 30%, and our results are about 25% lower than Dammann et al. (2019) estimates of the total coastal ice extent that include nonstabilized LFI zone. This fact requires further investigation and may be attributed to more conservative LFI identification using SAR interferometry than our approach with optical images.

Discussion and conclusions

Despite a long history of operational LFI mapping, some important issues related to detailed accuracy and climatology of the LFI in the Beaufort Sea region remain to be addressed. Several recent studies based on high-resolution satellite data pointed to a few important issues:

(1) Reported long-term trends, such as changes in the LFI spatial extent and timing parameters related to the LFI annual cycle, are not always consistent between different sources and may vary from one subregion to another due to regional climate variations (Galley et al. 2012; Mahoney et al. 2014; Yu et al. 2014; Li et al. 2020*b*; Trishchenko and Luo 2021);

(2) The typical width of the LFI zone along the coast at the peak season (April–May) in the Beaufort Sea ranges from less than 10 km to about 30 km (Mahoney et al. 2014; Trishchenko and Luo 2021). The outer edge of the LFI zone generally follows the 20–30 m isobaths;

(3) Reliable identification of the LFI zone requires multi-temporal data analysis that should include not only the ice concentration but also the assessment of ice stability, especially at the outer LFI edge (Dammann et al. 2019).

This study addresses some of these issues based on the approach developed by Trishchenko and Luo (2021) for the LFI mapping around Banks Island using MODIS 250 m imagery and extended it to the entire Beaufort Sea region. The 250 m spatial resolution imagery resolves very well the LFI spatial features with a typical size of several kilometres.

Monthly time series of the LFI parameters (spatial extent, average distance from the coast, and average water depth at the outer seaward edge) for 2000–2019 were produced for the April–September period each year. The statistics for water depth and distance of the outer seaward LFI edge from the coast were systematically derived for the entire Beaufort Sea region over a 20-year period for the first time to the best of our knowledge. Results were compared with the CIS ice charts and were found to be in good agreement. On average, the CCRS results showed systematic bias (6.7%) toward a smaller LFI area, as well as the shallower depth and shorter distance of the LFI edge from the coast. We attribute this to a better ability of the CCRS method to discriminate nonstabilized ice at the edge of the LFI zone.

Comparison of the Beaufort Sea region-wide LFI spatial extent derived in this study with data from Yu et al. (2014) also showed good agreement for January–May average value. This is a somewhat surprising finding taking into account that Yu et al. (2014) used a coarse resolution 25 km spatial grid, which cannot adequately resolve the LFI spatial features over most parts of the Beaufort Sea coastline, where the width of the LFI zone on average is below 30 km (Table 4), (Mahoney et al. 2014; Trishchenko and Luo 2021). The coarse-resolution data should likely lead to an underestimation of the LFI total area unless these data include accurate fractional values of LFI for each grid cell. The other possibility is that the Beaufort Sea boundary is defined over a larger region in Yu et al. (2014) than in our study. In fig. 1 of Yu et al. (2014), the weekly ice map over the Beaufort Sea region also included a large area of Amundsen Gulf which usually contains significant amounts of LFI. It is also possible that the coarse resolution data contain some uncertainties that lead to error compensation during the extrapolation of historical results. This hypothesis requires further investigation and re-analysis of historical CIS data at their original high spatial resolution.

The derived long-term trends in the LFI properties from different sources are generally consistent in detecting the overall negative trend in the LFI spatial extent over the entire Beaufort Sea region. However, they differ in the magnitude of the trend and assessment of its statistical significance. Yu et al. (2014) reported

a negative trend, −0.39 (±0.16) × 10^3 km^2 $year^{-1}$ (not significant at 0.05), for the January–May interval over the 1976–2007 period. Li et al. (2020*b*) reported −0.35 (±0.20) × 10^3 km^2 $year^{-1}$ trend for a similar parameter over the 1976–2018 period and found it statistically significant at 0.01 level, which is difficult to interpret taking into account that the stated magnitude and error should indicate even less statistical significance than the one reported by Yu et al. (2014). Our results also show the negative trend for the January–May period in 2000–2019, however, it is about four times smaller and is not statistically significant: −0.103 (±0.166) × 10^3 km^2/year (p = 0.54). Statistically significant negative trends are detected for the April–June multi-year time series: −4.45 (±1.69) × 10^3 km^2/decade (p = 0.02) and −4.73 (±2.17) × 10^3 km^2/decade (p = 0.04), from the CIS and the CCRS data, respectively (Table 2). The western part (Region 1: Alaska coast, Region 2: Barter–Hershel) shows a much smaller magnitude of trends than the eastern part (Region 3: Mackenzie Bay, Region 4: Richards–Bathurst). The eastern part because of its large size drives the trend for the entire Beaufort Sea.

Similar to Mahoney et al. (2014), our study confirms that 20–30 m isobaths generally correspond to the average position of the outer seaward LFI edge for the entire southern coastline of the Beaufort Sea and Banks Island regions (Regions 1–5) during the LFI peak season.

The long-term trends in the timing parameters of the LFI annual cycle show generally earlier break-up and the later freeze-up onset dates, and longer ice-free periods for the Beaufort Sea area. However, all these trends are not statistically significant, except the earlier break-up trend of −0.76 (±0.26) day/year (p = 0.01) for Region 3 (Mackenzie Bay). The declining LFI extent and trends in the timing parameters are generally consistent with the trends observed in the ERA5 surface air temperature at 2 m height (T2m) shown in Fig. 4. The large-scale analysis of the LFI properties across the Beaufort Sea region highlights the sensitivity of the Mackenzie Estuary (Region 3) to climate change. Improved accuracy of LFI mapping in this region, in particular, will enhance the safety, livelihood, and ability of the Inuvialuit people in this region to adapt.

The analysis of long-term monthly mean values and standard deviations of the LFI parameters combined with a visual inspection of time series at the original temporal resolution revealed a few large outliers in the CIS time series. These outliers correspond to rare cases of the CIS LFI maps that extend well beyond the average boundary. These anomalies may originate from the inclusion of nonstabilized ice with a high concentration located at the edge of the stable LFI zone into the landfast category.

Our study confirmed the advantage of using operational full-resolution maps of LFI at sub-kilometre spatial resolution for adequate studies of climatology in the Beaufort Sea region. The mapping consistency of LFI spatial features can also benefit from the multi-temporal analysis and availability of satellite imagery with high temporal frequency (Trishchenko and Garand 2011, 2012; Trishchenko et al. 2016*a*, 2019) that can better classify the areas of stabilized and nonstabilized LFI zones and their dynamics.

Acknowledgements

This work was conducted as part of the Climate Change Geoscience Program and CCRS Long-Term Satellite Data Records (LTSDR) activity as part of the Cumulative Effects project at CCRS, Department of Natural Resources Canada (NRCan). The authors gratefully acknowledge the use of MODIS data acquired from the NASA Distributed Archive Center and the ERA5 T2m data acquired from the European Copernicus data archive (https://cds.climate.copernicus.eu/cdsapp#!/home). The CIS charts were obtained from the CIS archive (https://iceweb1.cis.ec.gc.ca/Archive/). The CCRS LFI data are freely available at this link: ftp://ftp.ccrs.nrcan.gc.ca/ad/Trishchenko/BeaufortSeaLandfastIce.2000-2019/. The snow/ice probability map produced by the Canada Centre for Remote Sensing (CCRS) is available from the Canadian Federal Geospatial Platform (FGP) open-access public archive (https://open.canada.ca/data/en/dataset/808b84a1-6356-4103-a8e9-db46d5c20fcf). The manuscript was assigned the NRCan contribution number 20210273.

References

Babb, D.G., Galley, R.J., Barber, D.G., and Rysgaard, S. 2016. Physical processes contributing to an ice free Beaufort Sea during September 2012. Journal of Geophysical Research: Oceans, **121**: 267–283. doi:10.1002/2015JC010756.

Babb, D.G., Landy, J.C., Barber, D.G., and Galley, R.J. 2019. Winter sea ice export from the Beaufort Sea as a preconditioning mechanism for enhanced summer melt: A case study of 2016. Journal of Geophysical Research: Oceans, **124**: 6575–6600. doi:10.1029/2019JC015053.

Babb, D.G., Landy, J.C., Lukovich, J.V., Haas, C., Hendricks, S., Barber, D.G., and Galley, R.J. 2020. The 2017 reversal of the Beaufort Gyre: Can dynamic thickening of a seasonal ice cover during a reversal limit summer ice melt in the Beaufort Sea? Journal of Geophysical Research: Oceans, **125**: e2020JC016796. doi:10.1029/2020JC016796.

Barry, R.G., Moritz, R.E., and Rogers, J.C. 1979. The fast ice regimes of the Beaufort and Chukchi Sea coasts, Alaska. Cold Regions Science and Technology, **1**: 129–152. doi:10.1016/0165-232X(79)90006-5.

Beaudoin, A., Bernier, P.Y., Guindon, L., Villemaire, P., Guo, X.J., Stinson, G., Bergeron, T., et al. 2014. Mapping attributes of Canada's forests at moderate resolution through kNN and MODIS imagery. Canadian Journal of Forest Research, **44**(5): 521–532. doi:10.1139/cjfr-2013-0401.

Bernier, P.Y., Desjardins, R.L., Karimi-Zindashty, Y., Worth, D., Beaudoin, A., Luo, Y., and Wang, S. 2011. Boreal lichen woodlands: A possible negative feedback to climate change in eastern North America. Agricultural and Forest Meteorology, **151**(4): 521–528. doi:10.1016/j.agrformet.2010.12.013.

Betts, A.K., Desjardins, R., Worth, D., Wang, S., and Li, J. 2014. Coupling of winter climate transitions to snow and clouds over the Prairies. Journal of Geophysical Research, **119**(3): 1118–1139. doi:10.1002/2013JD021168.

Betts, A., Chan, D.Z., and Desjardins, R.L. 2019. Near-surface biases in ERA5 over the Canadian Prairies. Frontiers in Environmental Science, **7**: 129. doi:10.3389/fenvs.2019.00129.

Borodachev, V.E. 1998. L'dy Karskogo Morya. [Ice in the Kara Sea.] Gidrometeoizdat, St. Petersburg. ISBN 5-286-01373-2. 184pp.

Brodzik, M.J., and Knowles, K.W. 2002. Chapter 5: EASE-Grid: A versatile set of equal-area projections and grids. *In* Discrete global grids: a web book. *Edited by* M.F. Goodchild. National Center for Geographic Information & Analysis, Santa Barbara, California USA. Available from https://escholarship.org/uc/item/9492q6sm.

Carmack, E.C., and Chapman, D.C. 2003. Wind-driven shelf/basin exchange on an Arctic shelf: The joint roles of ice cover extent and shelf-break bathymetry. Geophysical Research Letters, **30**(14): 1778. doi:10.1029/2003GL017526.

Colditz, R.R., López Saldaña, G., Maeda, P., Espinoza, J.A., Tovar, C.M., Hernández, A.V., et al. 2012. Generation and analysis of the 2005 land cover map for Mexico using 250 m MODIS data. Remote Sensing of Environment, **123**: 541–552. doi:10.1016/j.rse.2012.04.021.

Colditz, R.R., Pouliot, D., Llamas, R.M., Homer, C., Ressl, R.A., Tovar, C.M., et al. 2014. Detection of North American land cover change between 2005 and 2010 with 250m MODIS Data. Photogrammetric Engineering and Remote Sensing, **80**(10): 918–924.

Cooley, S.W., Ryan, J.C., Smith, L.C., Horvat, C., Pearson, B., Dale, B., and Lynch, A.H. 2020. Coldest Canadian Arctic communities face greatest reductions in shorefast sea ice. Nature Climate Change, **10**(6): 533–538. doi:10.1038/s41558-020-0757-5.

Copernicus Climate Change Service (C3S). 2020. ERA5: Fifth generation of ECMWF atmospheric reanalyses of the global climate. Copernicus Climate Change Service Climate Data Store (CDS). Available from https://cds.climate.copernicus.eu/cdsapp#!/home [accessed on 25 September 2020].

Dammann, D.O., Eriksson, L.E., Mahoney, A.R., Eicken, H., and Meyer, F.J. 2019. Mapping pan-Arctic landfast sea ice stability using Sentinel-1 interferometry. Cryosphere, **13**: 557–577. doi:10.5194/tc-13-557-2019.

Divine, D., Korsnes, R., and Makshtas, A. 2003. Variability and climate sensitivity of land-fast ice extent in the north-eastern Kara Sea. Polar Research, **22**: 27–34. doi:10.3402/polar.v22i1.6440.

Eicken, H., Lovecraft, A.L., and Druckenmiller, M.L. 2009. Sea-ice system services: A framework to help identify and meet information needs relevant for Arctic observing networks. Arctic, **62**(2): 119–136. doi:10.14430/arctic126.

El-Alem, A., Chokmani, K., Laurion, I., and El-Adlouni, S.E. 2012. Comparative analysis of four models to estimate chlorophyll-*a* concentration in case-2 waters using MODerate resolution imaging spectroradiometer (MODIS) imagery. Remote Sensing, **4**(8): 2373–2400. doi:10.3390/rs4082373.

El-Alem, A., Chokmani, K., Laurion, I., and El-Adlouni, S.E. 2014. An adaptive model to monitor chlorophyll-*a* in inland waters in southern Quebec using downscaled MODIS imagery. Remote Sensing, **6**(7): 6446–6471. doi:10.3390/rs6076446.

El-Alem, A., Chokmani, K., Laurion, I., El-Adlouni, S.E., Raymond, S., and Ratte-Fortin, C. 2019. Ensemble-based systems to monitor algal bloom with remote sensing. IEEE Transactions on Geoscience and Remote Sensing, **57**(10): 7955–7971. doi:10.1109/TGRS.2019.2917636.

Environment and Climate Change Canada (ECCC). 2020. Ice chart descriptions. Available from https://www.canada.ca/en/environment-climate-change/services/ice-forecasts-observations/latest-conditions/products-guides/chart-descriptions.html [accessed 12 January 2020].

Fetterer, F., Savoie, M., Helfrich, S., and Clemente-Colón, P. 2010. Multisensor Analyzed Sea Ice Extent - Northern Hemisphere (MASIE-NH). 1-km resolution ice product. NSIDC: National Snow and Ice Data Center, Boulder, Colorado, USA. doi:10.7265/N5GT5K3K.

Flanders Marine Institute. 2019. Maritime boundaries geodatabase: Maritime boundaries and exclusive economic zones (200NM), version 11. Available from http://www.marineregions.org/.

Fontana, F.M.A., Trishchenko, A.P., Luo, Y., Khlopenkov, K.V., Nussbaumer, S.U., and Wunderle, S. 2010. Perennial snow and ice variations (2000-2008) in the Arctic circumpolar land area from satellite observations. Journal of Geophysical Research, **115**(4): F04020. doi:10.1029/2010JF001664.

Ford, J.D., Gough, W.A., Laidler, G.J., MacDonald, J., Irngaut, C., and Qrunnut, K. 2009. Sea ice, climate change, and community vulnerability in northern Foxe Basin, Canada. Climate Research, **38**: 137–154. doi:10.3354/cr00777.

Galley, R.J., Else, B.G.T., Howell, S.E.L., Lukovich, J.V., and Barber, D.G. 2012. Landfast sea ice conditions in the Canadian arctic: 1983-2009. Arctic, **65**(2): 133–144. doi:10.14430/arctic4195.

Gearheard, S., Matumeak, W., Angutikjuaq, I., Maslanik, J., Huntington, H.P., Leavitt, J., et al. 2006. It's Not that Simple: A collaborative comparison of sea ice environments, their uses, observed changes, and adaptations in Barrow, Alaska, USA, and Clyde River, Nunavut, Canada. Ambio, **35**: 203–211. doi:10.1579/0044-7447(2006)35[203:INTSAC]2.0.CO;2.

GEBCO Bathymetric Compilation Group 2020. 2020. The GEBCO_2020 Grid - a continuous terrain model of the global oceans and land. British Oceanographic Data Centre, National Oceanography Centre, NERC, UK. doi:10.5285/a29c5465-b138-234d-e053-6c86abc040b9. Available from https://www.bodc.ac.uk/data/published_data_library/catalogue/10.5285/a29c5465-b138-234d-e053-6c86abc040b9/.

Gignac, C., Bernier, M., Chokmani, K., and Poulin, J. 2017. IceMap250-automatic 250 m sea ice extent mapping using MODIS Data. Remote Sensing, **9**(1): 70. doi:10.3390/rs9010070.

Global Climate Observing System (GCOS). 2016. The global observing system for climate: Implementation needs. GCOS–200. 341pp. Available from https://gcos.wmo.int/en/home [accessed 25 September 2020].

Hanesiak, J.M., Stewart, R.E., Bonsal, B.R., Harder, P., Lawford, R., Aider, R., et al. 2011. Characterization and Summary of the 1999–2005 Canadian Prairie Drought. Atmosphere-Ocean, **49**(4): 421–452. doi:10.1080/07055900.2011.626757.

Hersbach, H., Bell, B., Berrisford, P., Hirahara, S., Horányi, A., Muñoz-Sabater, J., et al. 2020. The ERA5 global reanalysis. Quarterly Journal of the Royal Meteorological Society, **146**(730): 1999–2049. doi:10.1002/qj.3803.

Huntington, H.P., Gearheard, S., Holm, L.K., Noongwook, G., Opie, M., and Sanguya, J. 2016. Sea ice is our beautiful garden: Indigenous perspectives on sea ice in the Arctic. *In* Sea ice. 3rd ed. John Wiley and Sons. pp. 583–599. doi:10.1002/9781118778371.ch25.

International Hydrographic Organization (IHO). 1953. Limits of oceans and seas. 3rd ed. Special Publication No. 4223 (S-23). International Hydrographic Organization, Monaco. 42pp.

JCOMM. 2014. SIGRID-3: A Vector Archive Format for Sea Ice Charts. Version 3.0. JCOMM Technical Report No. 23/WMO/Technical Document No. 1214. World Meteorological Organization, Geneva, Switzerland 40pp. Available from https://www.jcomm.info/index.php?option=com_oe&task=viewDocumentRecord&docID=4439.

Ji, L., Wylie, B., Ramachandran, B., and Jenkerson, C. 2010. A comparative analysis of three different MODIS NDVI datasets for Alaska and adjacent Canada. Canadian Journal of Remote Sensing, **36**(1): S149–S167. doi:10.5589/m10-015.

Jin, X., Hanesiak, J.M., and Barber, D.G. 2007. Time series of daily averaged cloud fractions over landfast first-year sea ice from multiple data sources. Journal of Applied Meteorology and Climatology, **46**(11): 1818–1827. doi:10.1175/2007JAMC1472.1.

Karvonen, J. 2018. Estimation of Arctic land-fast ice cover based on dual-polarized Sentinel-1 SAR imagery. The Cryosphere, **12**(8): 2595–2607. doi:10.5194/tc-12-2595-2018.

Khlopenkov, K.V., and Trishchenko, A.P. 2008. Implementation and evaluation of concurrent gradient search method for reprojection of MODIS level 1B imagery. IEEE Transaction on Geoscience and Remote Sensing, **46**(7): 2016–2027. doi:10.1109/TGRS.2008.916633.

Laidre, K.L., and Regehr, E.V. 2016. Arctic marine mammals and sea ice. *In* Sea ice. 3rd ed. *Edited by* D.N. Thomas. John Wiley and Sons. pp. 516–533. doi:10.1002/9781118778371.ch21.

Laidre, K.L., Stirling, I., Lowry, L.F., Wiig, O., Heide-Jorgensen, M.P., and Ferguson, S.H. 2008. Quantifying the sensitivity of Arctic marine mammals to climate-induced habitat change. Ecological Applications, **18**(2): S97–S125. doi:10.1890/06-0546.1.

Li, Q., Zhou, C., Zheng, L., Liu, T., and Yang, X. 2020*a*. Monitoring evolution of melt ponds on first-year and multiyear sea ice in the Canadian Arctic Archipelago with optical satellite data. Annals of Glaciology, **61**(82): 154–163. doi:10.1017/aog.2020.24.

Li, Z., Zhao, J., Su, J., Li, C., Cheng, B., Hui, F., et al. 2020*b*. Spatial and temporal variations in the extent and thickness of Arctic landfast ice. Remote Sensing, **12**(1): 64–20pp. doi:10.3390/rs12010064.

Liu, J., Worth, D.E., Desjardins, R.L., Haak, D., McConkey, B., and Cerkowniakdet, D. 2020. Influence of two management practices in the Canadian Prairies on radiative forcing. Science of the Total Environment, **11**: 142701. doi:10.1016/j.scitotenv.2020.142701.

Liu, Y., Wang, Z., Sun, Q., Erb, A.M., Li, Z., Schaaf, C.B., et al. 2017. Evaluation of the VIIRS BRDF, Albedo and NBAR products suite and an assessment of continuity with the long term MODIS record. Remote Sensing of Environment, **201**: 256–274. doi:10.1016/j.rse.2017.09.020.

Loseto, L.L., Hoover, C., Ostertag, S., Whalen, D., Pearce, T., Paulic, J., et al. 2018. Beluga whales (*Delphinapterus leucas*), environmental change and marine protected areas in the Western Canadian Arctic. Estuarine, Coastal and Shelf Science, **212**: 128–137. doi:10.1016/j.ecss.2018.05.026.

Luo, Y., Trishchenko, A.P., and Khlopenkov, K.V. 2008. Developing clear-sky, cloud and cloud shadow mask for producing clear-sky composites at 250-meter spatial resolution for the seven MODIS land bands over Canada and North America. Remote Sensing of Environment, **112**(12): 4167–4185. doi:10.1016/j.rse.2008.06.010.

Mahoney, A.R. 2018. Landfast sea ice in a changing Arctic. *In* Arctic Report Card 2018. *Edited by* E. Osborne, J.A. Richter-Menge, and M.O. Jeffries. pp. 99–109. [National Oceanic and Atmospheric Administration, 2018.] Available from https://arctic.noaa.gov/Portals/7/ArcticReportCard/Documents/ArcticReportCard_full_report2018.pdf [accessed on 16 June 2021].

Mahoney, A.R., Eicken, H., Gaylord, A.G., and Shapiro, L. 2007*a*. Alaska landfast sea ice: links with bathymetry and atmospheric circulation. Journal of Geophysical Research, Oceans, **112**: C02001. doi:10.1029/2006jc003559.

Mahoney, A.R., Eicken, H., and Shapiro, L. 2007*b*. How fast is landfast sea ice? A study of the attachment and detachment of nearshore ice at Barrow, Alaska. Cold Regions Science and Technology, **47**(3): 233–255. doi:10.1016/j.coldregions.2006.09.005.

Mahoney, A.R., Eicken, H., Gaylord, A.G., and Gens, R. 2014. Landfast sea ice extent in the Chukchi and Beaufort Seas: The annual cycle and decadal variability. Cold Regions Science and Technology, **103**: 41–56. doi:10.1016/j.coldregions.2014.03.003.

Mäkynen, M., Karvonen, J., Cheng, B., Hiltunen, M., and Eriksson, P.B. 2020. Operational Service for Mapping the Baltic Sea Landfast Ice Properties. Remote Sensing, **12**: 4032. doi:10.3390/rs12244032.

Manual of Ice (MANICE). 2009. Canadian Ice Service. Environment and Climate Change Canada. Available from https://www.canada.ca/en/environment-climate-change/services/weather-manuals-documentation/manice-manual-of-ice.html [accessed on 15 October 2020].

Melling, H. 2002. Sea ice of the northern Canadian Arctic Archipelago. Journal of Geophysical Research, **107**(C11): 3181–3121. doi:10.1029/2001JC001102.

Meyer, F.J., Mahoney, A.R., Eicken, H., Denny, C.L., Druckenmiller, H.C., and Hendricks, S. 2011. Mapping arctic landfast ice extent using L-band synthetic aperture radar interferometry. Remote Sensing of Environment, **115**(12): 3029–3043. doi:10.1016/j.rse.2011.06.006.

Mundy, C.J., Gosselin, M., Ehn, J., Gratton, Y., Rossnagel, A., Barber, D.G., et al. 2009. Contribution of under-ice primary production to an ice-edge upwelling phytoplankton bloom in the Canadian Beaufort Sea. Geophysical Research Letters, **36**: L17601. doi:10.1029/2009GL038837.

Mundy, C.J., Gosselin, M., Gratton, Y., Brown, K., Galindo, V., Campbell, K., et al. 2014. Role of environmental factors on phytoplankton bloom initiation under landfast sea ice in Resolute Passage, Canada. Marine Ecology Progress Series, **497**: 39–49. doi:10.3354/meps10587.

Nghiem, S.V., Hall, D.K., Rigor, I.G., Li, P., and Neumann, G. 2014. Effects of Mackenzie River discharge and bathymetry on sea ice in the Beaufort Sea. Geophysical Research Letters, **41**(3): 873–879. doi:10.1002/2013GL058956.

Overeem, I., Anderson, R.S., Wobus, C.W., Clow, G.D., Urban, F.E., and Matell, N. 2011. Sea ice loss enhances wave action at the Arctic coast. Geophysical Research Letters, **38**: L17503. doi:10.1029/2011GL048681.

Overland, J.E., Hanna, E., Hanssen-Bauer, I., Kim, S.-J., Walsh, J.E., Wang, M., et al. 2019. Surface air temperature. *In* Arctic Report Card 2019. *Edited by* J. Richter-Menge, M.L. Druckenmiller, and M. Jeffries. 100 pp. Available from https://arctic.noaa.gov/Report-Card/Report-Card-2019.

Platnick, S., King, M., and Hubanks, P. 2015. MODIS atmosphere L3 monthly product. NASA MODIS adaptive processing system, Goddard Space Flight Center. doi:10.5067/MODIS/MOD08_M3.061.

Proshutinsky, A., Bourke, R.H., and McLaughlin, F.A. 2002. The role of the Beaufort Gyre in Arctic climate variability: seasonal to decadal climate scales. Geophysical Research Letters, **29**(23): 2100. doi:10.1029/2002GL015847.

Ratté-Fortin, C., Chokmani, K., and El-Alem, A. 2018. A novel algorithm of cloud detection for water quality studies using 250 m downscaled MODIS imagery. International Journal of Remote Sensing, **39**(19): 6429–6439. doi:10.1080/01431161.2018.1460506.

Ratté-Fortin, C., Chokmani, K., and Laurion, I. 2020. Spatiotemporal variability in phytoplankton bloom phenology in Eastern Canadian lakes related to physiographic, morphologic, and climatic drivers. Environments, **7**(10): 77. doi:10.3390/environments7100077.

Salomonson, V.V., Barnes, W.L., Maymon, P.W., Montgomery, H.E., and Ostrow, H. 1989. MODIS: Advanced facility instrument for studies of the earth as a system. IEEE Transactions on Geoscience and Remote Sensing, **27**(2): 145–153. doi:10.1109/36.20292.

Steele, M., Dickinson, S., Zhang, J., and Lindsay, R. 2015. Seasonal ice loss in the Beaufort Sea: Toward synchrony and prediction. Journal of Geophysical Research: Oceans, **120**: 1118–1132. doi:10.1002/2014JC010247.

Stubenrauch, C.J., Rossow, W.B., Kinne, S., Ackerman, S., Cesana, G., Chepfer, H., et al. 2013. Assessment of global cloud datasets from satellites: Project and database initiated by GEWEX radiation panel. Bulletin of the American Meteorological Society, **94**(7): 1031–1049. doi:10.1175/BAMS-D-12-00117.1.

Talbot, S.S., and Meades, W.J., 2011. Circumboreal Vegetation Map (CBVM): Mapping the green halo. Concept Paper. CAFF Strategy. Series Report No. 3. CAFF Flora Group (CFG), CAFF International Secretariat, Akureyri, Iceland. ISBN 978-9935-431-05-9. Available from https://www.caff.is/monitoring-series/50-circumboreal-vegetation-map-cbvm-mapping-the-green-halo-concept-paper/download.

Tivy, A., Howell, S.E.L., Alt, B., McCourt, S., Chagnon, R., Crocker, G., et al. 2011. Trends and variability in summer sea ice cover in the Canadian Arctic based on the Canadian Ice Service Digital Archive, 1960–2008 and 1968–2008. Journal of Geophysical Research, **116**: C03007. doi:10.1029/2009JC005855.

Trishchenko, A.P. 2019. Clear-Sky Composites over Canada from Visible Infrared Imaging Radiometer Suite: Continuing MODIS Time Series into the Future. Canadian Journal of Remote Sensing, **45**(3–4): 276–289. doi:10.1080/07038992.2019.1601006.

Trishchenko, A.P. 2020. Probability of the annual minimum snow and ice (MSI) presence over Canada. Dataset. Version 4. Available from https://open.canada.ca/data/en/dataset/808b84a1-6356-4103-a8e9-db46d5c20fcf.

Trishchenko, A.P., and Garand, L. 2011. Spatial and temporal sampling of polar regions from two-satellite system on Molniya orbit. Journal of Atmospheric and Oceanic Technology, **28**: 977–992. doi:10.1175/JTECH-D-10-05013.1.

Trishchenko, A.P., and Garand, L. 2012. Observing polar regions from space: Advantages of a satellite system on a highly elliptical orbit versus a constellation of low earth polar orbiters. Canadian Journal of Remote Sensing, **38**(1): 12–24. doi:10.5589/m12-009.

Trishchenko, A.P., and Luo, Y. 2021. Landfast ice mapping using MODIS clear-sky composites: Application for Banks Island coastline in Beaufort Sea and comparison with Canadian Ice Service data. Canadian Journal of Remote Sensing, **47**(1): 143–15816. doi:10.1080/07038992.2021.1909466.

Trishchenko, A.P., and Ungureanu, C. 2021. Minimum snow/ice extent over the Northern Circumpolar Landmass in 2000–19: How much snow survives the summer melt? Bulletin of the American Meteorological Society, **102**(4): E748–E764. doi:10.1175/BAMS-D-20-0177.1.

Trishchenko, A.P., and Wang, S. 2018. Variations of climate, surface energy budget and minimum snow/ice extent over Canadian Arctic landmass for 2000-16. Journal of Climate, **31**(3): 1155–1172. doi:10.1175/JCLI-D-17-0198.1.

Trishchenko, A.P., Luo, Y., and Khlopenkov, K.V. 2006. A method for downscaling MODIS land channels to 250 m spatial resolution using adaptive regression and normalization. *In* Proceedings of SPIE Int. Soc. Opt. Eng. Vol. 6366. p. 636607. doi:10.1117/12.689157.

Trishchenko, A.P., Luo, Y., Khlopenkov, K.V., Park, W.M., and Wang, S. 2009. Arctic circumpolar mosaic at 250 m spatial resolution for IPY by fusion of MODIS/TERRA land bands B1–B7. International Journal of Remote Sensing, **30**(6): 1635–1641. doi:10.1080/01431160802348119.

Trishchenko, A.P., Garand, L., Trichtchenko, L.D., and Nikitina, L.V. 2016*a*. Multiple-apogee highly elliptical orbits for continuous meteorological imaging of polar regions. Bulletin of the American Meteorological Society, **97**(1): 19–24. doi:10.1175/BAMS-D-14-00251.1.

Trishchenko, A.P., Leblanc, S.G., Wang, S., Li, J., Ungureanu, C., Luo, Y., et al. 2016*b*. Variations of annual minimum snow and ice extent over Canada and neighboring landmass derived from MODIS 250-m imagery for 2000–2014. Canadian Journal of Remote Sensing, **42**(3): 214–242. doi:10.1080/07038992.2016.1166043.

Trishchenko, A.P., Garand, L., and Trichtchenko, L.D. 2019. Observing polar regions from space: Comparison between highly elliptical orbit and medium Earth orbit constellations. Journal of Atmospheric and Oceanic Technology, **36**(8): 1605–1621. doi:10.1175/JTECH-D-19-0030.1.

Wang, X., and Key, J.R. 2005. Arctic surface, cloud, and radiation properties based on the AVHRR Polar Pathfinder dataset. Part I: Spatial and temporal characteristics. Journal of Climate, **18**(14): 2558–2574. doi:10.1175/JCLI3438.1.

Way, R.G., and Lewkowicz, A.G. 2016. Modelling the spatial distribution of permafrost in Labrador–Ungava using the temperature at the top of permafrost. Canadian Journal of Earth Sciences, **53**(10): 1010–1028. doi:10.1139/cjes-2016-0034.

World Meteorological Organization (WMO). 2014. WMO sea-ice nomenclature. WMO- No. 259, 121 pp. Available from https://library.wmo.int/index.php?lvl=notice_display&id=6772 [accessed on 12 June 2021].

Xiong, X., Che, N., and Barnes, W. 2005. Terra MODIS on-orbit spatial characterization and performance. IEEE Transactions on Geoscience and Remote Sensing, **43**(2): 355–365. doi:10.1109/TGRS.2004.840643.

Xiong, X., Che, N., Barnes, W., Xie, Y., Wang, L., and Qu, J. 2006. Status of Aqua MODIS spatial characterization and performance. *In* Proceedings of SPIE International Society for Optical Engineering, 6361, 63610T. 9 pp. doi:10.1117/12.687162.

Yu, Y., Stern, H., Fowler, C., Fetterer, F., and Maslanik, J. 2014. Interannual variability of arctic landfast ice between 1976 and 2007. Journal of Climate, **27**(1): 227–243. doi:10.1175/JCLI-D-13-00178.1.